nature reviews methods primers

https://doi.org/10.1038/s43586-024-00323-5

Primer

Check for updates

Tip-enhanced Raman scattering

Christiane Höppener[1,2], Javier Aizpurua[3,4,5], Huan Chen[6], Stefanie Gräfe[1,7], Ado Jorio[8], Stephan Kupfer[1], Zhenglong Zhang[6] & Volker Deckert[1,2]

Abstract

Tip-enhanced Raman scattering (TERS) is one of the few methods to access the molecular composition and structure of surfaces with extreme lateral and depth resolution, down to the nanometre scale and beyond. This Primer examines the underlying physical principles driving signal enhancement and lateral resolution of TERS, laying the foundation for both theoretical understanding and practical applications. Addressing critical factors such as reproducibility, averaging and general limitations, we delve into the nuances of TERS experiments. Various TERS modifications are introduced, highlighting diverse optical geometries and tip feedback schemes tailored to the specific experimental needs. State-of-the-art TERS studies are showcased to illustrate its versatility, encompassing structural analysis of biomolecules, nanoscale investigation of chemical reactivity and exploration of the intrinsic physical properties of 2D materials. These TERS applications serve as a comprehensive overview of current advancements in the field, encapsulating the breadth of TERS experiments.

Sections

[1]Institute of Physical Chemistry and Abbe Center of Photonics, Friedrich-Schiller University, Jena, Germany. [2]Leibniz Institute of Photonic Technology, Jena, Germany. [3]Donostia International Physics Center DIPC, Donostia-San Sebastián, Spain. [4]Ikerbasque, the Basque Foundation for Science, Bilbao, Spain. [5]Department of Electricity and Electronics, EHU/UPV, Donostia-San Sebastián, Spain. [6]School of Physics and Information Technology, Shaanxi Normal University, Xi'an, China. [7]Fraunhofer Institute for Applied Optics and Precision Engineering, Jena, Germany. [8]Departamento de Física, Universidade Federal de Minas Gerais, Minas Gerais, Brazil. e-mail: volker.deckert@uni-jena.de

Introduction

Tip-enhanced Raman scattering (TERS) is a powerful vibrational probing technique combining the inherent spectroscopic abilities of Raman scattering with substantial signal amplification and exceptional spatial resolution achieved through localized optical fields at the scattering tip apex[1–3]. Unlike other optical near-field microscopy techniques, TERS enables chemical imaging with sub-molecular spatial resolution. The localized optical fields at the plasmonic tip lead to strong enhancement of otherwise weak Raman signals, amplifying them by several orders of magnitude, thus enabling sensitivity down to the single molecule[4–6]. This unique combination offers chemical specificity, allowing the resolution of vibrational signatures of materials and molecular species even at the subnanometre range[7].

TERS facilitates the experimental exploration of the molecular structures of surface-bound molecules, overcoming the resolution limitations of diffraction optics by operating within the near-field optical regime. The signal amplification in TERS arises from the enhancement of the non-resonant or resonant excitation at a defined wavelength. As a result, lateral resolutions much finer than conventional optical microscopes can be achieved, reaching single-molecule or sub-molecular sensitivity. Understanding the underlying physical mechanisms driving TERS applications at the nanometre and subnanometre scales has led to continuous theoretical advancements in describing the specific contributions to signal amplification, even within a quantum mechanical framework.

The remarkable TERS capabilities were initially demonstrated through detailed investigations into intrinsic material properties of condensed matter and structural properties of biomolecules, such as high-resolution studies of carbon nanotubes[8,9] revealing chirality changes[10], defect identification[11] and strain probing[12,13]. Similar aspects are now being explored in TERS studies of a variety of 2D materials[14]. TERS is also highly valuable for studying molecular interactions[15–19], molecular monolayers[20,21], molecular orientations[22], biopolymers such as peptides, proteins and fibrils[23–31], polymer films and nanostructures[32–36], as well as nanoscale chemical reactions[37–42]. This Primer focuses on selected applications in solid-state physics, chemical reactivity and biological nanoscale analysis to illustrate the broad scale of potential applications.

Theoretical description of TERS

To understand the remarkable resolution and enhancement properties of TERS theoretically, various electromagnetic and chemical interactions must be considered.

The enhancement in TERS involves two main contributions. First, the electromagnetic enhancement results from locally confined and intensified enhanced electric fields and gradients near a metal interface, typically resonantly enhanced owing to plasmonic modes in specific geometrical configurations, such as the plasmonically active tip apex used in TERS. This enhancement substantially improves the Raman signal of molecular species within this near field. Second, chemical interactions arise from close-range, site-specific interactions between the surface-bound sample and the metallic nanoparticle. These interactions include non-resonant and resonant contributions, as well as charge-transfer phenomena between the sample and the plasmonic nanoparticle. Such charge-transfer processes are particularly prominent at close tip–sample distances and when sample molecules are adsorbed on metallic surfaces; they modify the electronic structure of the molecule when located near the plasmonic subsystem. In surface–sample interactions, such charge-transfer processes are mainly modulated by the surface properties of the given plasmonic metal and by the binding mode, particularly the orientation of the adsorbed sample molecule with respect to the surface. Owing to very accurate positioning of the plasmonic tip with respect to the sample molecule, site-specific interactions lead to the modification of the local chemical environment affecting the electronic structure of the plasmonic hybrid system. These tip–molecule site-specific spectral modifications contribute to further enhancement of the lateral resolution.

Optical properties of a plasmonic tip

The strong and ultra-resolved Raman signal obtained from scattering tips is attributed to ability of metallic probes to localize electromagnetic fields below the diffraction limit. This localization arises from the collective response of the electrons to the incoming light, which sustains electromagnetic resonances and produces localized surface plasmon excitations at the tip apex. These excitations serve to confine propagating light into tiny effective mode volumes around the nanostructure, thus overcoming the diffraction limit. Owing to this light localizing and enhancing effect, metallic nanostructures have been often called optical nanoantennas, with different geometrical configurations developed to tailor the wavelength and properties of the local field associated to these resonances. Commonly used nanostructures include nanorods, nanoshells, nanodimers, nanogaps and metallic tips. The optical response and localization of electromagnetic fields around metallic tips can be modelled using methods such as finite element methods[43], finite-difference time-domain methods[44] or boundary element methods[45,46] (Fig. 1a). The field enhancement produced by a typical metallic tip (radius of ~20 nm) is approximately 10-fold larger than the incident field below the tip apex. This enhancement can be intensified when the tip is located on a metallic surface, generating a coupled plasmonic gap[47]. Although the enhancing power of a standard plasmonic gap is remarkable, this alone is not capable of explaining the ultrahigh spatial resolution (<1 nm) recently achieved. Atomic-scale protrusions at the tip are capable of further confining light to single atoms, with a threefold to fivefold signal enhancement[48,49], leading to the term picocavity to refer to atomic-scale light localizing features of these atomic protrusions[50,51]. The use of picocavities in scanning tips has enabled state-of-the-art TERS experiments where intramolecular vibrational features are now routinely resolved[52–55].

Chemical aspects of tip–sample interaction

Chemical effects become prominent at close tip–sample ranges (<1 nm), forming site-specific hybrid systems of metal atoms from the plasmonic tip and the sample molecule (Fig. 1b). These effects include ground state interactions between the tip and sample, resonance contributions and from charge-transfer phenomena, collectively referred to as non-resonant, resonant and charge-transfer contributions, respectively. Theoretical approaches[48,51,56–66], such as the discrete interaction model or quantum mechanical model[60–62], combine time-dependent density functional theory (TDDFT) simulations for the molecular sample with atomistic electrodynamics simulations for the nanoparticle to model such plasmon-molecule hybrid systems accurately. Charge-transfer contributions are particularly relevant at close tip–sample distances, influencing resolution and plasmon-induced catalysis. Incorporating sufficient metal atoms from the tip at short tip–molecule distances into the quantum chemistry is essential for an accurate description of charge-transfer states in scanning tunnelling microscopy (STM)-TERS studies.

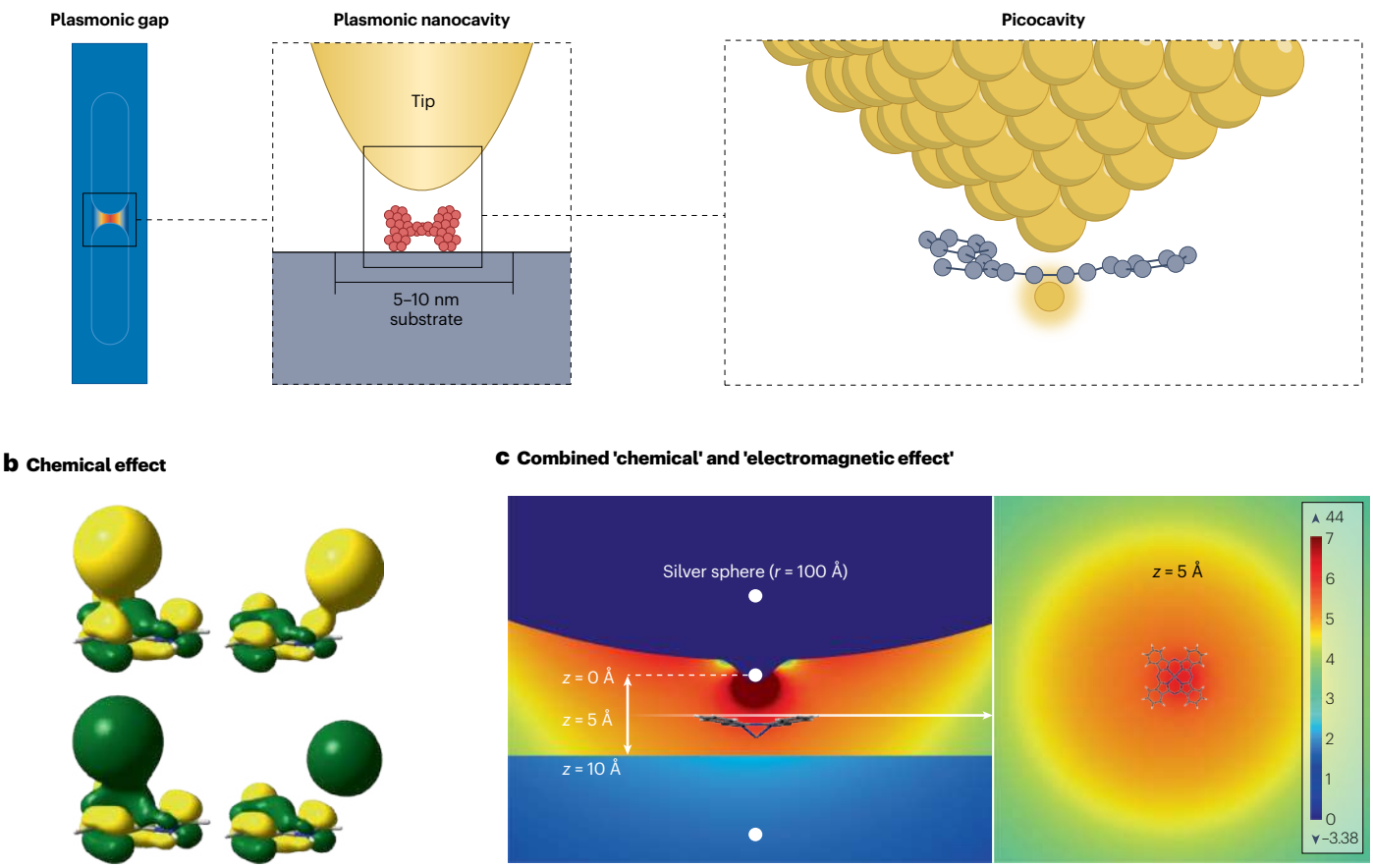

Fig. 1 | Simulation of plasmon-enhanced Raman signals, combining electromagnetic and chemical enhancement. a, Scaled interactions of an illuminated tip: nanoscale enhancement owing to a gap formation between two plasmonic particles; additional field enhancement owing to atomic-scale protrusions (picocavities); representation of the strong localization of a picocavity (here with an additional gap mode); full representation of extreme field localization with respect to a molecule[184]. **b**, Site-specific local chemical interactions between sample and plasmonic tip, mimicked by a single silver atom and a sample molecule (*xy* plane). Three-dimensional grid calculations with varying tip–sample positions are performed to chemically map the localized interaction of the sample with the plasmonic tip. For the shown adenine molecule, the chemical effect stems from locally enforced molecule–tip configurations, based on the overlap of the semi-occupied silver orbital and the π-system of adenine. At larger (*z*-)distances, the electromagnetic effect dominates the modulation of the Raman signal. **c**, A full description of the chemical and electromagnetic effects can be obtained by incorporating the electric near-field, which can be obtained by finite-element method simulations, into the quantum chemical simulation. As a model, a tin(II) phthalocyanine molecule is placed below the tip as shown in *xz* and *xy* plane (left and right, respectively). Part **b** reprinted from ref. 67, CC BY 3.0. Part **c** adapted with permission from ref. 80, American Chemical Society.

When simulating TERS and resonance Raman spectra[67–70], the plasmonic tip scanning over the substrate can be represented by an individual metal atom or a small cluster, such as the Ag_{20} and Au_{20} clusters[69,71,72]. At each relative tip–sample position, the electronic structure is calculated using quantum-chemical methods such as density functional theory (DFT) for non-resonant terms and TDDFT for resonance and charge-transfer terms, as well as the corresponding Raman and possibly resonance Raman spectra[67,70,73,74]. These calculations enable tracking of potential site-specific changes in the electronic structure and the occurrence of charge-transfer states. This includes characteristics such as metal-to-molecule charge-transfer, which can result in a partially positively or negatively charged tip, inducing dipole moments, bond order changes and the energetic position of the state. If electronically excited states are energetically close to the incident wavelength in the experiment, both non-resonant Raman and resonance Raman spectra need to be calculated, as these contribute substantially to resonance excitation[69,70,75]. Notably, the properties of charge-transfer states are highly sensitive to the local tip–molecule interaction, in particular if polarized along the electric field, whereas locally excited states of the sample are typically less affected by chemical modifications induced by the metallic nanoparticle. The combination of these contributions generates a TERS map of the molecule, facilitating chemical imaging.

Electromagnetic and chemical effects

The electromagnetic and chemical contributions to TERS have traditionally been treated separately. However, recent approaches have

aimed to integrate these contributions to understand their combined impact on signal enhancement, spatial resolution and chemical specificity. Hybrid multi-scale calculations, such as those using the GPAW code[76,77], allow for the inclusion of electromagnetic near-fields into electronic structure calculations at the tip–sample interface[78–80]. Additionally, methods have been developed to incorporate the effect of strongly inhomogeneous local fields, such as those in picocavities formed by atomic protrusions, into quantum calculation of the Raman polarizability tensor[81]. This captures the effects of inhomogeneous fields but misses important quantum effects connected with charge-transfer to the metal. Alternatively, the near-field around the tip apex including atomic-scale protrusions can first be calculated[43,51,82,83] using a standard Maxwell's equation solver[43]. The resulting near-field is represented by carefully placed point charges, which can be included in the quantum chemical calculations, enabling the assessment of the impact of the near-field on the electronic structure and the corresponding Raman spectra[80]. The sample molecule is subsequently mapped by the tip and the local field that follows the tip position (Fig. 1c), disentangling the effects of the metal proximity's chemical contribution, the electromagnetic near-field and the combination of both. Such analysis shows that particularly the charge-transfer states are affected when including the contribution of the electromagnetic field. This approach has demonstrated that the atomic-scale site sensitivity originates from chemical effects while incorporating the electromagnetic near-field leads to an additional overall enhancement of the signal[80].

This Primer aims to provide a concise introduction of the current theoretical and experimental aspects of TERS. As applications continue to diversify, ranging from nanoscale compound identification to the investigation of chemical reactivity, the selected results achieved using TERS represent the current state-of-the-art in this evolving field. Finally, general challenges inherent in working with sample volumes deviating from bulk behaviour are addressed.

Experimentation

Instrumentation

TERS experiments typically involve mapping a region of interest using a TERS tip in a predefined pattern to record the Raman signal at specified positions. The number of pixels of the pattern usually determines the lateral resolution, ensuring that the resulting step size is equal to or smaller than the lateral confinement at the tip apex. TERS instrumentation consists of an optical setup to excite and collect the scattered Raman signal, either in transmission or reflection mode, and a tip–sample manipulation system to precisely control the movement of the tip with subnanometre precision (Fig. 2).

The optical setup includes an illumination system to focus laser light with controlled polarization onto the apex of a plasmonic tip, a collection system to gather the scattered light while suppressing unwanted contributions using suitable filter and a detection system. Various illumination schemes have been developed to accommodate sample and spatial constraints (Box 1). Plasmonic nanofocusing-based tip concepts have been introduced[84–86] to separate the bulk excitation volume from the nanoconfined excitation volume at the tip apex, effectively suppressing background noise (Box 2). Spatial coherence and momentum matching of the incident field can be achieved through adaptive optics[87], enhancing light coupling to the tip[88,89]. The use of a fixed or tunable excitation wavelength depends on experimental requirements, with fixed being the most frequent approach, and excitation-dependent TERS using the tunable approach enabling, for instance, the distinguishing of species with varying optical transitions[90]. Similarly to all Raman spectroscopies, optical filter combinations are crucial for rejecting unwanted wavelengths — such as cleaning the excitation wavelength — and suppressing the Rayleigh line in the detection path[91,92].

TERS signal detection can involve capturing full spectroscopic information using a charge-coupled device (CCD) camera-coupled spectrograph or focusing on intensity maps of specific marker bands using a single-point photodetector. The latter approach accelerates data acquisition times, enabling mapping at smaller step sizes within acceptable acquisition times. Faster acquisition time trades off with the amount of information obtained, as information encoded in the entire spectrum — such as the band shifting related to specific bond conformations — is lost. Careful consideration of total recording time is necessary to address the effects of mechanical and thermal drift, particularly in ambient and liquid environments. Additional drift compensation approaches can be optionally implemented into TERS setups. These use in situ drift correction to maintain the tip within the optimal illumination volume, enabling ultra-stable tip-enhanced scattering conditions for robust long-term mapping and imaging over large sample areas and at sufficiently small step sizes. Both lateral drift compensation of the tip position and axial focus drift correction systems rely on a feedback-controlled piezoelectric actuation to adjust the tip or focus position, relying on optical readouts[93–96] such as Rayleigh scattering at the tip.

The second sub-system of a TERS microscope deals with the precise spatial manipulation of the tip and the sample. Lateral manipulation of the sample is achieved using a close-loop piezoelectric scanner, while maintaining the vertical tip position usually relies on the principles of atomic force microscopy (AFM)[97] or scanning tunnelling microscopy (STM)[98].

AFM-based TERS. In AFM-TERS the tip–sample distance is regulated by probing the normal forces, such as short-range repulsive Coulomb interactions[99], attractive van der Waals interactions and superimposed long-range electrostatic and capillary forces (Fig. 2). Alternatively, shear-force interactions[100] between the tip apex and the sample can be used, offering the advantage of eliminating the need for an additional light source for control.

Force detection involves sensitive force sensors, such as cantilevers or piezoelectric quartz tuning forks. A sensitive feedback loop controls the vertical tip–sample distance and prevents the tip from crashing into the sample (Fig. 2). Contact and non-contract AFM operation modes are distinguished based on the applicable tip–sample interaction[97,101,102] (Fig. 2), with their impact TERS signal enhancement outlined in Box 3.

Long-range capillary forces are a frequent issue under ambient conditions, and can strongly influence feedback and the minimum stable tip–sample distance. This can be addressed by moving from ambient conditions to ultrahigh-vacuum (UHV) or liquid environments. In the latter case, additional liquid-substrate and liquid-cantilever force interactions generally require different feedback parameters to maintain a stable tip–sample distance.

STM-based TERS. STM-based TERS uses precise positioning and gap separation distances provided by the tunnelling current between a conductive tip and a conductive sample. Applying a bias voltage between tip and sample generates a net electron flow that is highly dependent on the distance between them, allowing for a very stable tip–sample distance regulation via a feedback loop. Although

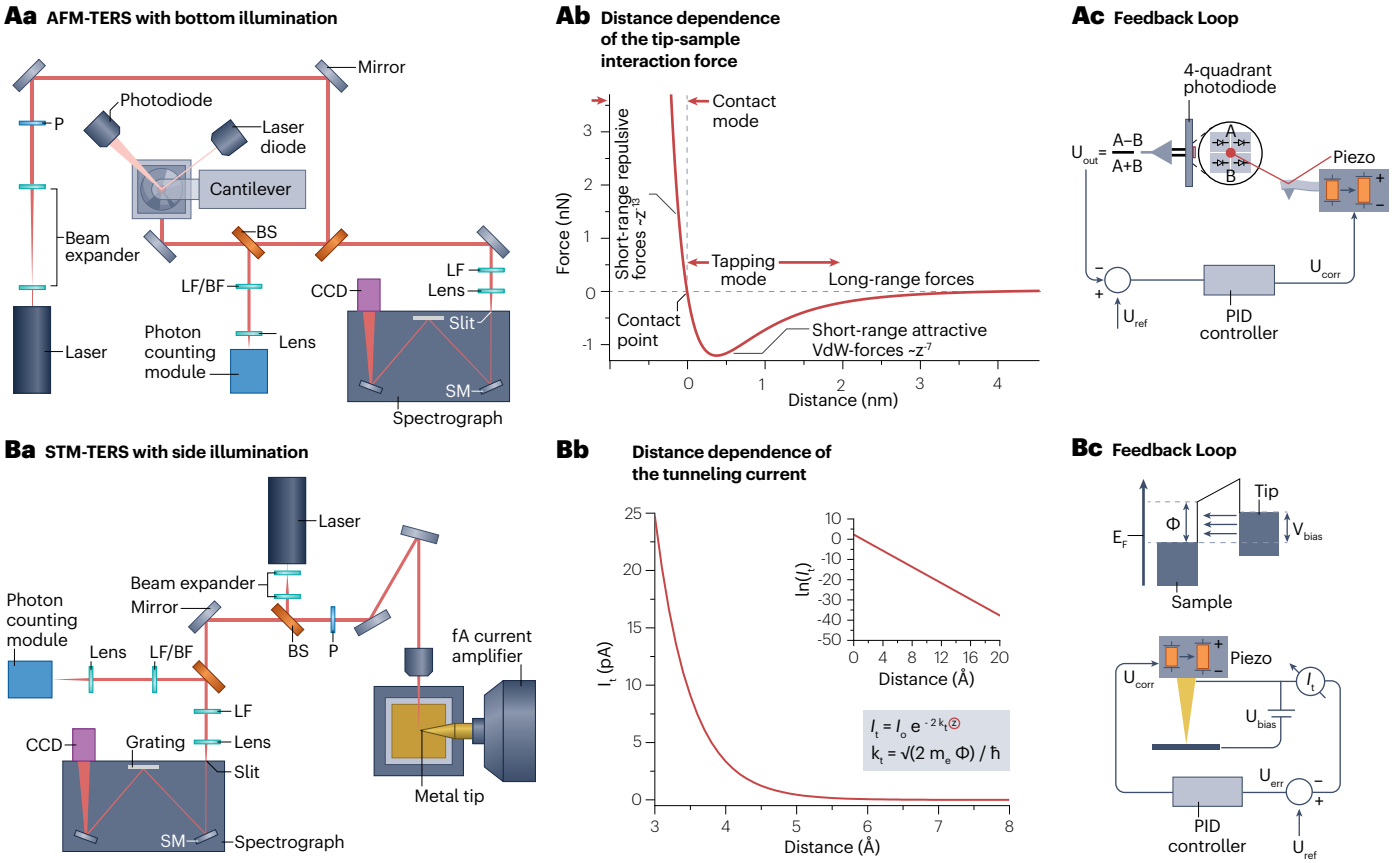

Fig. 2 | TERS setup configurations. A, Transmission mode AFM-TERS (atomic force microscopy combined with tip-enhanced Raman scattering spectroscopy), with bottom illumination. **B**, Reflection mode STM-TERS (scanning tunnelling microscopy combined with tip-enhanced Raman scattering spectroscopy) with side illumination. **Aa**,**Ba**, Outline of the respective excitation, collection and detection path, based on stable narrow linewidth laser, a beam expander often in the form of a spatial filter, polarization optics (P) for laser mode conversion (optional), and an objective to tightly focus the laser beam to the tip–sample area and to collect the scattered Raman signal. The collected signal is either focused onto the active area of a photodiode (point detection) or is focused onto the entrance slit of the spectrograph for spectrally resolved multichannel detection. **Ab**,**Bb**, Distance dependence of the non-monotonically varying force (top) and monotonically changing tunnelling current I_t (bottom) used as a feedback signal in AFM and STM. **Ac**,**Bc**, Outline of AFM (part **Ac**) and STM (part **Bc**) feedback loop to control the tip–sample distance. A bias voltage U_{bias} is applied to shift the Fermi-level E_F of the tip and sample to enable electron tunnelling. The measured sensor signal is compared with a predefined reference signal U_{ref} (set point). After amplification, this signal is further processed in a feedback loop (here, a proportional-integral-differential (PID) controller), yielding an accurate correction function U_{corr}, resulting in a sensitive and stable tip–sample distance with subnanometre precision. BS, dichroic beam splitter; CCD, charge-coupled device; LF/BF, ultra-steep edge long pass or band pass filters; SM, spherical mirror; U_{err}, error signal; vdW, van der Waals.

STM-TERS and AFM-TERS use different physical properties, both achieve similar experimental feedback. However, STM-TERS is limited to conductive substrates or very thin non-conductive samples on conductive substrates.

Comparing the two TERS systems, AFM-based TERS offers flexibility, applicability to various sample types and environments, large scanning ranges and fast scanning speeds. By contrast, STM-TERS systems provide greater stability, making tip–sample distances easier to control. Both systems can achieve subnanometre resolution and single-molecule level sensitivity[53,54], with further improvement possible in low-temperature and high-vacuum environment. The UHV environment eliminates the competitive adsorption interference of air impurities and slows down the photobleaching of samples, reduces the thermal drift of the sample and improves the stability of the system. Although, sub-molecular resolution currently has been demonstrated only for STM cryogenic UHV conditions, prospectively (sub-)molecular-resolved TERS might be achieved with AFM-based modalities and ambient conditions in the future.

TERS tip concepts

The quality of the tip directly impacts the resolution and image quality of scanning probe microscopy (SPM) and TERS measurement. Parameters such as tip material, curvature radius, cone angle and surface morphology substantially influence TERS sensitivity by affecting plasmon resonance and electromagnetic field intensity. These parameters usually depend on the fabrication method and the precision at the nanometre scale, and are tuneable via the size and shape of the plasmonic tip, respectively. TERS enhancement is generally greater when the tip surface plasmon resonances match the excitation and/or emission wavelength, and tips with sharp ends and smooth surfaces

dissipate less heat. Various tip designs have evolved to control these parameters[103], using fabrication methods such as focused ion beam milling, electrochemical etching methods[104], physical vapour deposition and e-beam lithography. Simple shearing of wires is the easiest machining method, albeit lacking reproducibility, whereas electrochemical etching methods produce tips with the desired aspect ratios and surface conditions by adjusting etching voltage, etching solution composition and concentration and wire immersion[105]. Here subsequent formation of metal atomic clusters can further enhance spatial resolution; tips are usually bombarded with argon ions, then heated with electron beams and modified on the flat metal surface of the single crystal. This strategy is most often used for STM-TERS tips. Physical vapour deposition methods reliably produce TERS active tips, however, intrinsically the precise localized plasmon resonances are variable. which is overcome by introducing nanostructures at the tip apex, such as thin silver film resulting in AgNP-decorated tips or plasmonic cavities[106–108]. The incorporation of picocavities at the tip end can provide Ångström-scale resolution and electromagnetic field enhancement, albeit with reduced lifetime under ambient conditions[109].

To extend the lifespan of the tip, a dense protective layer is occasionally applied to the metal tip[110–113]. Additionally, to minimize leakage currents from the tip of STM-TERS at the liquid–solid interface, the tip may be coated with substrates such as polyethylene paraffin wax, zapon or nail polish[114,115].

Box 1 | Basic TERS illumination schemes

Side or top illumination (preferred in STM-TERS)

- Thick and opaque samples
- Long working distance, low numerical aperture (NA) objectives
- Direct (oblique) sample irradiation
  - Strong Raman background signal
  - Restriction to a Gaussian laser mode
  - Low light coupling and collection efficiency
  - Poor image quality, owing to non-vertical arrangement of the imaging path and the sample–tip
- Alternative use of a parabolic mirror[185] (not shown in the figure) to avoid the low NA drawbacks

Bottom illumination (preferred in AFM-TERS)

- Thin and (semi-)transparent samples
- Applicability of high NA objectives (≫1)
- Applicability of higher-order vortex beams
  - Tightly focused laser spots
  - Strong longitudinal field components
  - Reduced direct sample irradiation and smaller Raman background signal
  - Higher signal-to-noise ratio
  - Higher light coupling and collection efficiency

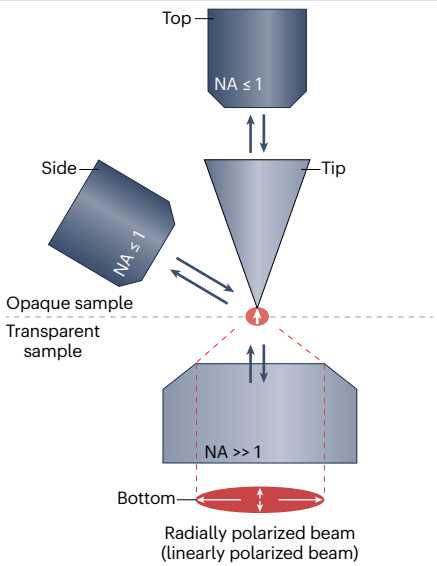

AFM, atomic force microscopy; STM, scanning tunnelling microscopy; TERS, tip-enhanced Raman scattering.

Data recording and processing

Modern SPM controllers facilitate fast acquisition channels, accumulating transistor–transistor logic (TTL) output signals from point detectors for intensity mapping as a function of the tip position. Full spectral information acquisition requires synchronization of tip motion and spectrum acquisition, typically achieved through handshaking procedures. The communication between the SPM and optical detection units involves TTL signals defining the start and stop signals for the optical data acquisition. Various software tools are used for data correction, storage and analysis. Self-written Matlab programs or commercial software packages such as Vista Control software are used to correlate individually recorded TERS spectra with the AFM tip position. SPM data are stored in controller brand-specific data file formats. Several freeware data analysis software tools, such as Gwyddion[116], can be used for data treatment and statistical evaluation of parameters. TERS spectra are stored usually as text files and are subject to univariate and multivariate data analysis. Combined with quantum-chemical calculations, assignment of Raman bands can identify the composition and orientation of certain compounds.

Results

TERS experiments target specific material properties and functions based on spectroscopic frameworks derived from preliminary experimental and theoretical data sets or archived Raman spectroscopy databases. The TERS spectrum of a compound should resemble the peak pattern of the corresponding conventional bulk Raman spectrum, although the tip can slightly influence spectra, and also the number of molecules observed in an experiment may not provide an average result. Therefore, displaying unprocessed, representative TERS spectra is recommended to obtain an unbiased estimate and rule out potential experimental influences.

Tip-induced spectral deviations

TERS spectral patterns can deviate from conventional Raman spectra owing to tip-induced variations. Additional instrument-specific Raman bands can arise; for example, silicon cantilever-based tips produce peaks at 520 cm^{-1} and ~900–1000 cm^{-1}, corresponding to the silicon phonon band and its overtone, respectively (Fig. 3a). Serious issues arise from tip aging, damage and inefficient light coupling, leading to a gradual or abrupt signal intensity loss and affecting the signal-to-noise ratio (SNR). Transiently emerging or remaining undesired Raman bands caused by molecules temporally or permanently residing at the tip apex or on the tip shaft can be confused with desired surface-specific Raman

Box 2 | Advanced TERS modes for enhancing the sensitivity and stability

Plasmon nanofocusing[84–86,186–189]

- Applicable to a broad wavelength range
- Spatial separation of the bulk excitation volume from the nanoconfined sample irradiation
- Use of integrated surface plasmon–polariton (SPP) couplers, for example, grating, cavities and photonic crystals
- Gradual compression and propagation of the excited SPPs to the tip apex along the tapered tip shaft in the limit of adiabatic SPP damping
- SPP amplitude enhances along the propagation direction
  - Nanoscale energy compression of the incident light into volumes of only several cubic nanometres
  - Spot size is determined by the atomic structure of the tip and the non-local electronic response (spatial dispersion)
  - Efficient background suppression
  - Low energy losses
  - SPP propagation depends critically on taper angle and length of the tip, metal film thickness, and material properties of the metal–dielectric interface
- Minimization of energy losses demands for smooth metal surfaces
- Sophisticated nanofabrication tools with nanoscale accuracy are required

Adaptive illumination[87,190]

- Momentum and phase matching according to the atomistic structure of the tip–sample
- Compensation of distortions of the laser focus upon transmission through thick samples and samples with varying index of refraction (IoR)
- Iterative adjustment processes based on the optimization of a tip-induced reference signal, for example, tip-enhanced luminescence
  - Tip-enhanced Raman scattering (TERS) with nearly perfect laser beam profiles
  - Improvement of the light coupling efficiency and TERS signal stability
  - High signal-to-noise ratios achievable

marker bands. Tip contamination is hallmarked by exceptionally high peak intensities which obscure these Raman bands. Permanent tip contamination can be assessed by retracting the tip 10–100 nm from the sample surface or by comparing with a TERS substrate spectrum and identifying whether the signal persists.

Various factors, including sample degradation and tip–plasmon-induced reactions, can lead to additional peaks in the TERS spectra. For example, the dimerization of *p*-nitrothiophenol (pNTP) to 4,4′-dimercaptoazobenzene (DMAB)[37,38,117–119] may show vibrational bands of the newly formed azo group after the dimerization of pNTP, whereas pNTP-specific modes decrease or completely disappear (Fig. 3a). Sample degradation owing to light irradiation can cause significant artificial changes in a TERS spectrum, which are not representative for the analyte. Plasmon-induced charge-driven dissociation has been identified as a major degradation mechanism for biological samples such as peptides and proteins[120]. Thermal dissociation may occur at very high laser powers. Sample burning of organic compounds is often accompanied by strongly fluctuating peak patterns and the appearance of broad bands at 1350 cm^{-1} and 1570 cm^{-1} associated to the G-band and D-band of carbonaceous species[121,122]. Other TERS spectral deviations from Raman bulk spectra can be attributed to modified Raman selection rules thus, non-active Raman modes can become active owing to strong transverse and longitudinal field gradients[87,123–126], which couple to quadrupole–quadrupole interactions. Particularly, adaptive optical irradiation schemes demonstrated that infrared-active Raman modes can be selectively turned on and off through phase modulation[87].

In a TERS experiment, the absence of certain vibrational modes and differences in the intensity ratio of certain marker bands can be influenced by specific excitation conditions. TERS tips that provide strong electromagnetic field enhancement factors typically generate strong longitudinal field components. These components are orthogonal to the substrate and sample plane, and mainly excite vibrational modes associated in this direction, whereas in-plane vibrational mode enhancement, typical for normal Raman microscopy, is less efficient[127]. Altered TERS spectra may arise also from the confined information depth, resulting in the absence of specific Raman marker bands owing to shielding effects of certain functional residues in macromolecules[128]. Additionally, shifts in the peak position in TERS spectra may occur owing to metal–molecule charge-transfer mechanisms, particularly evident when chemical enhancement becomes non-neglectable in TERS investigations using the STM point contact regime[129,130]. These effects, tied to the high resolution capabilities of TERS, enable conclusions regarding the immediate vicinity of the molecule under investigation.

Standardization and quality control

Standardization of TERS experiments is crucial to ensure independent information gathering and to achieve high-quality, reproducible and comparable experimental data. Standardization involves following well specified sample preparation protocols and measurement routines commonly used in Raman and surface-enhanced Raman spectroscopy and in scanning probe microscopy. Particularly routine reference measures and protocols, such as choosing a suitable feedback mode and illumination–detection configuration, as well as adjustable procedures to adapt to experiment and sample properties. Careful adjustment of laser power density, wavelength and data integration time per spectrum is necessary to optimize the SNR and prevent sample damage. Additionally, obtaining a statistically meaningful number of spectra per area is essential for reproducibility. Beam alignment and spectrometer calibration must be monitored on a regular basis to ensure data comparability.

Quality control of experimental datasets is necessary, and it is important to adhere to routine referencing and assignment for Raman and scanning probe microscopies. This involves impartially evaluating the TERS data based on SNR. Only high-quality data should be considered for reliable postprocessing. Each spectrum is inspected for outliers and potential tip-induced alterations to obtain a set of marker bands representative of a pristine TERS spectrum. Raman data analysis may be hindered by detector sensitivity to cosmic rays, leading to occasional spikes in intensity, which can be identified by their

Box 3 | Impact of different feedback modes on the TERS signal enhancement

In scanning tunnelling microscopy (STM) and atomic force microscopy (AFM) contact modes, the tip remains continuously at a distance ≪1 nm, resulting in a nearly constant electromagnetic field enhancement across the entire signal integration time. For an AFM shear-force mode, the small lateral oscillation of the tip (oscillation amplitude ≪1 nm) does not affect the vertical tip position; therefore, the tip continuously remains at much larger distances (>1 nm), leading to lower enhancement capabilities. For the tapping mode AFM feedback, the tip–sample distance changes across a range from <1 nm (contact regime) to over 5 nm, according to the applied oscillation amplitude. Consequently, the obtainable enhancement continuously changes from high to low, and it only remains for a minor period of the total signal integration time in the optimal tip–sample distance regime associated with a maximum signal enhancement. Utilizing a tapping mode–feedback mode leads to an average signal enhancement much lower than for the AFM or STM contact modes[191], at lower mechanical stress[192]. Hence, to obtain a good signal enhancement, the oscillation amplitude of the tip should be reduced as much as possible while enabling stable feedback conditions. Alternatively, time-gated illumination or detection modes synchronized with the tip motion can be applied to record the TERS signal only for the small tip–sample distances near the contact point.

TERS signal enhancement	Tapping mode	Shear-force mode (AFM)	Contact mode (AFM)	Constant current (STM)
Tip oscillation amplitude	≥5 nm, vertical	≪1nm, lateral	–	–
Minimum tip–sample distance	<1 nm	~1 nm	≪1 nm	≪1 nm
Effective tip–sample distance	0–6 nm	~1 nm	≪1 nm	≪1 nm
Signal enhancement	5–75%	<50%	100%	~90%

The effective TERS signal enhancement critically depends on the applied feedback mode to control and maintain the tip–sample distance, owing to the vertical tip–sample distance dependence[43].

ultranarrow band width and often removed without losing information. Spectra normalization can mitigate experimentally induced intensity variations caused by laser power fluctuations, mechanical drifts or variations in tip enhancement capabilities. These fluctuations affect tip-specific bands, which can be used for peak intensity normalization. Alternatively, Raman bands independent of molecular conformational or environmental changes can be used in spectra normalization.

Baseline correction procedures can address the non-homogenous background in TERS spectra arising from substrate illumination, fluorescence emission and electronic noise from the CCD camera chip. This can be done by subtracting the substrate's TERS spectrum obtained under the same experimental conditions as for the analyte sample. Ideal baseline correction involves procedures at each image or mapping pixel, the acquisition of a regular TERS spectrum and a Raman spectrum recorded at a retracted tip position (Fig. 3b). Alternative methods such as asymmetric least square smoothing, derivative or nonlinear interactive peak clipping algorithms can be used. However, these post-processing steps carry the risk of causing unwanted TERS spectra modifications and should be applied cautiously, preferably only with high quality data to avoid over fitting.

TERS data analysis

Owing to various experimental effects on TERS spectra, displaying unprocessed TERS spectra for initial assessment is recommended. Data analysis focuses on identifying peak patterns from molecular functional groups via specific peak parameters such as wavenumber position, intensity and peak width. Individual peaks are fitted with a Lorentzian or mixed Lorentzian–Gauss function. The fitted positions, intensity ratios and widths of all peaks ideally well match the raw spectra and allow to draw conclusions regarding molecular orientations and tip–sample interactions. The fitting of a band provides quantitative information about the numerical peak parameters, although direct relation to structural parameters is generally not possible, instead requiring molecular modelling approaches.

Univariate data analysis extracts information on selected Raman bands in the form of averages and distributions. Advanced analysis methods, such as multivariate data analysis methods[27,54], reduce data dimensionality and extract relevant information from TERS spectra, owing to the high correlation of some Raman bands that share the same source of variation[131,132].

TERS correlation with other properties

Understanding the collective and cooperative properties of, and the roles of electrical and mechanical forces involved in these processes, is crucial for comprehending material behaviour and limitations. In recent years, there has been a focus on the development of multimodal and correlative approaches in various fields. These approaches offer the potential to enrich our understanding of molecular processes by considering complementary sample properties or using different spatial or time resolution capabilities.

Initially aimed at elucidating chemical composition and structure of materials, TERS has evolved to serve as a fundamental platform for multimodal and correlative investigations when combined with AFM and STM modes; these combined techniques provide synchronous information into chemical composition, structural properties, sample topology and mechanical and electronic properties. The addition of other standalone methodologies, such as micro-Raman spectroscopy, nano-infrared (nano-IR) spectroscopy, tip-enhanced photoluminescence and electron microscopy is also useful for extracting additional information. These integrated approaches using TERS as a pivotal method paired with complementary techniques are termed synergistic TERS.

A crucial aspect of synergistic TERS approaches lies in the spatial resolution capabilities of the paired methodologies. Although analytical methods yielding information exceeding the nanoscale sampling volume of TERS typically aim at a discrimination between different species or morphology differences within materials, direct correlation of quantitative measure and chemical composition is often redundant owing to this mismatch. However, this approach presents new strategies for extracting information from nanoscale objects that is not accessible by using either technique alone, relying on a qualitative comparative approach. For example, the presence or absence of certain marker bands in TERS, with its shallow information depth,

can distinguish surface-related materials and structures from bulk properties. This differs and complements nano-IR or micro-Raman techniques, which offer deeper information depths of several ten nanometres and several hundred nanometres, respectively.

By contrast, quantifying material properties becomes meaningful when paired methods yield nearly identical information depth, typically observed in scanning probe-based techniques. These techniques enable direct correlation between quantified surface properties and the chemical composition and molecular assembly of the surface. Data interpretation aims to understand how chemical composition, structure and molecular assembly influence electrical and mechanical properties, and vice versa. Such synergistic information is crucial for optimizing electrical and mechanical transport properties. Although synergistic TERS modalities are still in their early stages of development, recent case studies highlight their great potential[35,36,133–136].

Case studies. Of particular interest are synergistic AFM-TERS (Fig. 4a) and AFM force volume spectroscopy investigations (Fig. 4b). The latter allows quantitative monitoring of the nanomechanical properties of materials by recording force–distance curves for each imaging pixel[102]. The stiffness of the specimen can be determined from the strain curve by analysing the linear part of the branch associated with the repulsive tip–sample interaction, corresponding to elastic deformation. In other words, stiffer samples result in steeper curves. Young's modulus can be calculated using appropriate contact models, whereas adhesion force is determined by measuring the minimum of the retraction branch of the force curve. These quantities can be accessed with nanoscale lateral resolution. When combined with TERS, these properties can be interpreted in terms of the chemical composition, conformational changes and molecular assembly.

Synergistic AFM-TERS has been used to study the core crosslinking process initiated by a furan–maleimide Diels–Alder reaction within the confined core region of core–corona block copolymer micelles[35]. Information obtained on the chemical composition and the structure of the block copolymer chains from the evolving marker band intensity and position across the interfacial region was paired with the quantitively determined the stiffness, Young's modulus and adhesion of the core, corona and core–corona interface from force–volume AFM spectroscopy (Fig. 4c). This enabled the identification of influences affecting the crosslinking efficiency across the entire core region associated with highly crosslinked polymer chains facilitated by a high density of furan moieties and sequestered crosslinker molecules, which was supported by the TERS data. Conversely, a breakdown of the crosslinking process was observed at the interface between the glycidyl–polyethylene oxide core and corona owing to the exclusion of the crosslinker from this region, resulting in a decreasing Young's modulus towards the core-shell interfacial region. The efficiency of the crosslinking process appeared to be influenced by the degree of intermixing between the hydrophilic polyethylene oxide and the hydrophobic furfuryl-glycidyl ether block in this region, leading to higher chemical heterogeneity and altered nanomechanical properties in the interfacial region (Fig. 4c). This synergistic AFM-TERS study provided in-depth insights into how structure–property relations control molecular processes in confined spaces.

STM-TERS is particularly useful when combined with electrochemistry, known as electrochemical (EC)-TERS[137–139]. EC-TERS uses a bi-potentiostat to control the electrochemical environment and monitor chemical changes through TERS, allowing for correlation between the structure of electrochemical interfaces and their properties and functionality, which are governed by various processes such as molecular absorption[140], desorption and diffusion, surface reconstruction, charge-transfer, bond formation and chemical reactions[141]. Another example of synergistic TERS is correlative TERS-KPFM (Kelvin probe force microscopy) studies, which pair chemical properties with the contact potential difference and capacitance of surfaces. These studies are particularly useful for analysing 2D materials in terms of local defect density[133], spatial distribution of grain boundaries and their charge carrier concentration[142].

Applications

This section showcases the versatility of TERS in investigating a wide range of materials across disciplines. Through state-of-the-art studies, we illustrate various analytical and experimental aspects relevant to studying materials in the fields of biological and life sciences, chemistry and solid-state physics. The selected applications demonstrate the strength of TERS in identifying and discriminating nanoscale organic materials, characterizing intrinsic material properties of both common 1D and 2D materials and driving chemical reactions at the nanoscale at smallest length scales.

Biological applications

TERS has garnered considerable interest for its ability to probe biological matter with low or moderate Raman scattering cross-sections, offering high sensitivity and chemical specificity[143]. TERS can discern major biomolecular components such as genetic materials, proteins,

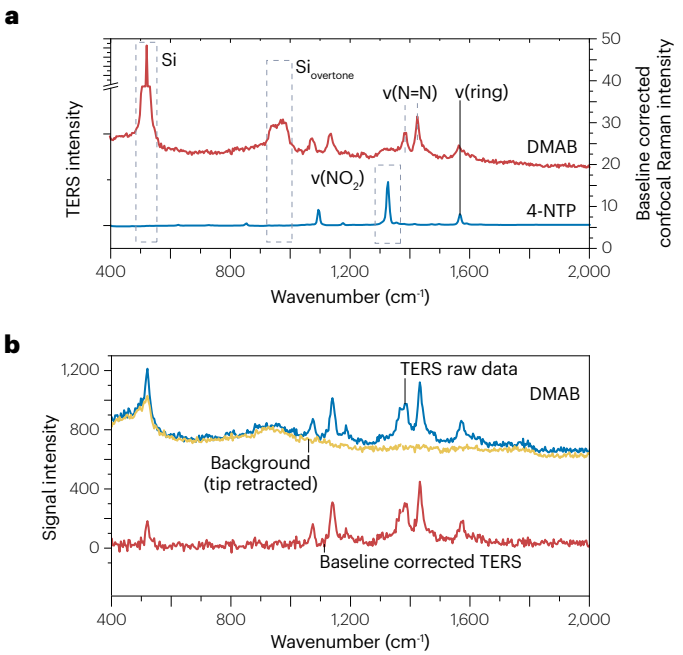

Fig. 3 | Different processes and parameters determining the TERS peak pattern and deviations from bulk Raman spectra. a, Comparison of a tip-enhanced Raman scattering (TERS) spectrum recorded with a silver nanoparticle-decorated Si-atomic force microscopy cantilever tip and a bulk Raman spectrum of 4-nitrothiophenol (4-NTP). Differences in the peak pattern arise from tip-specific modes (the silicon band at 520 cm^{-1} and its overtone at ~950 cm^{-1}) and plasmon-induced reaction (the dimerization of 4-NTP to dimercaptoazobenzene (DMAB)). **b**, Baseline correction of a recorded TERS spectrum of DMAB by subtraction of a background spectrum recorded after retraction of the tip.

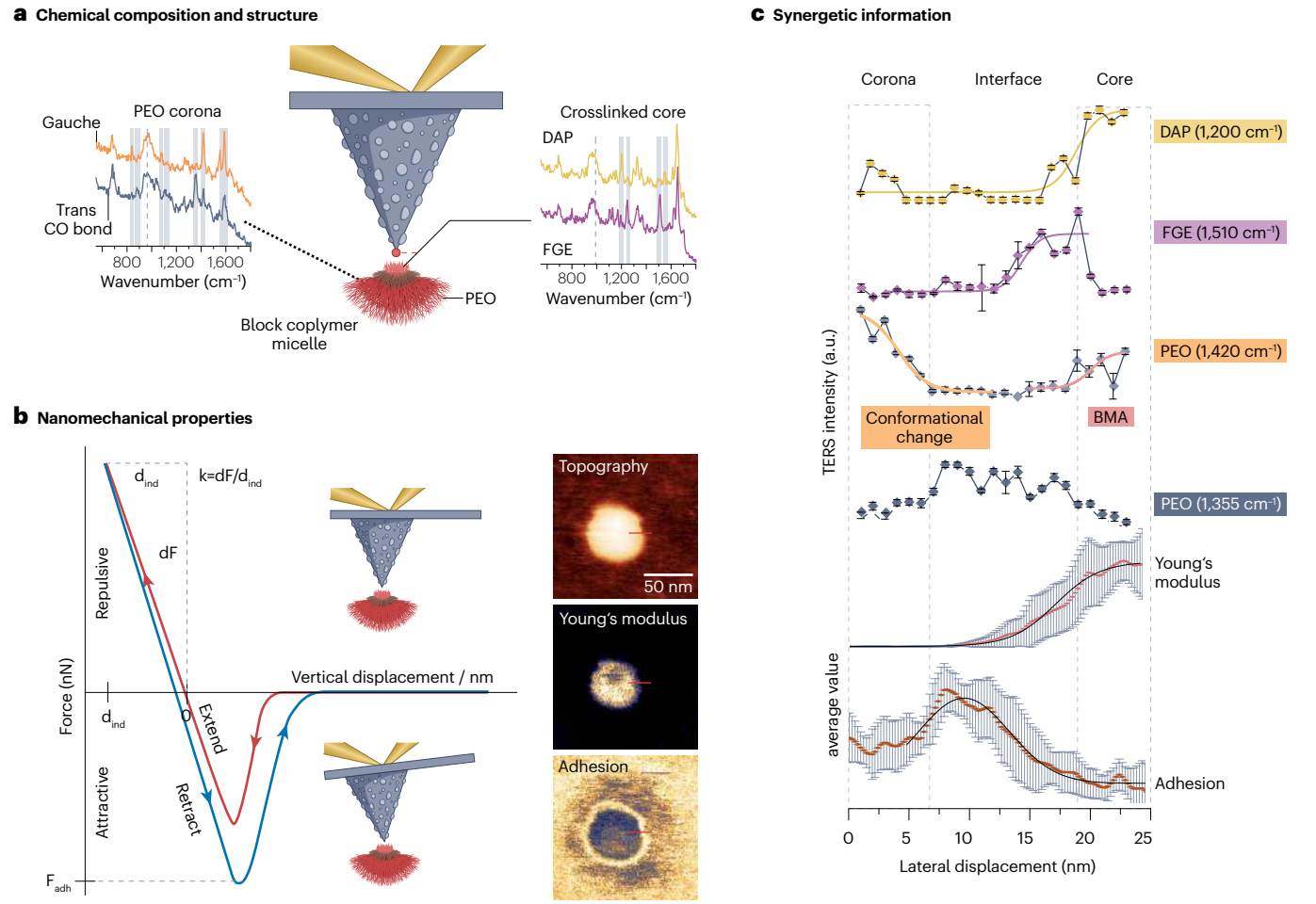

Fig. 4 | Synergistic TERS for correlating the chemical composition and nanomechanical properties of core crosslinked block copolymer core–corona micelles. a, Tip-enhanced Raman scattering (TERS) of fractured PEO-*b*-P(FGE-*co*-tBGE) micelles identifies corona-specific polyethylene oxide (PEO) and core-specific furfuryl-glycidyl ether (FGE) and Diels–Alder product (DAP) marker bands. **b**, Force–volume atomic force microscopy of the fractured micelles provide information on the nanomechanical properties across the entire micelle area. Topography, adhesion and Young's modulus images reveal a stiff, hydrophobic core region, indicating a high crosslinking efficiency and a soft hydrophilic corona region, which are separated by a highly hydrophilic interfacial area with lower crosslinking efficiency. **c**, Cross-sections across the interfacial region reveal a high compartment selective chemical distribution of the PEO and glycidyl-ether blocks, a high crosslinking efficiency in the central core region (DAP), and quantitatively correlate these to the modified nanomechanical properties. a.u., arbitrary units; BMA, 1,1′-(methylenedi-4,1-phenylene)-bis-maleimide. Adapted with permission from ref. 35, Wiley.

lipids and carbohydrates based on the specific Raman marker bands associated with each group. It enables identification of molecular orientations, various electronic, hydration and hybridization states, *cis* or *trans* isomerization, and can provide information on secondary or tertiary structure of peptides and proteins. TERS studies offer insights into various biological processes, including membrane morphogenesis, lipid raft formation, cell polarization and signalling pathways, glycosylation, inflammation, interfacial cargo transport, drug–target interactions, protein misfolding and toxicity. The technique holds promise for advancing understanding in fields such as treatment of cancer and infectious diseases.

A prominent area using TERS focuses on the structure, polymorphism and formation of protein fibres[23–28], their toxicity – particularly of amyloid fibres[29–31] – and their interaction with lipids[31,144]. However, studying biological materials often requires controlled environmental conditions to preserve function. Currently, TERS studies of biological matter in its native state owing to challenges in liquid AFM-TERS are challenging[145]. Research targeting extracellular vesicles, cell membranes and tissues have been primarily conducted under ambient conditions[146–151].

RNA and DNA sequencing. TERS, with its Ångström-scale lateral resolution, is being explored as a tool for sequencing RNA, DNA, peptides and proteins. It can distinguish individual nucleobases and amino acids without labelling strategies or material amplification, enabling detection at picomolar levels[152,153]. TERS has been successful in label-free detection and sequencing of single-stranded and double-stranded DNA and RNA oligomers by identifying variations in nucleobase marker[154–159]. Single-nucleobase resolution was achieved using TERS on M13mp13 phage single-stranded DNA (ssDNA)[160] and single-stranded RNA (ssRNA). This was accomplished with a step size of 0.5 nm in a gap mode configuration,

wherein the sample was sandwiched between a flat gold substrate and the tip, followed by multivariate data analysis for classification[161] (Fig. 5Aa,Ab). A sequencing accuracy of >90% was obtained because occasional interferences with adjacent nucleobases can occur in their tight arrangement (Fig. 5Ac). Furthermore, differentiation of DNA hybridization states is feasible through observation of backbone-specific

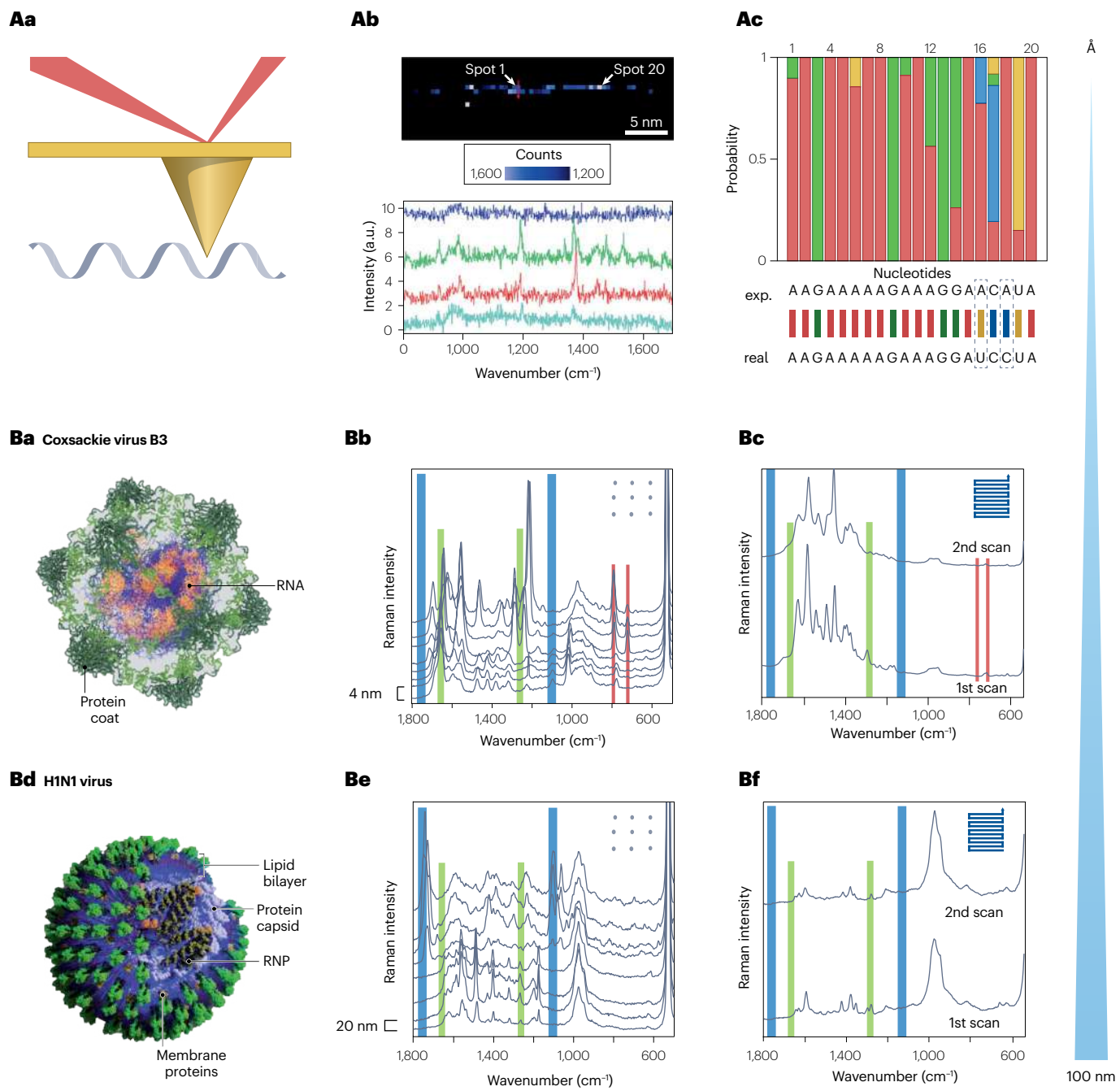

Fig. 5 | Application of TERS spectroscopy to biological samples. A, Single-stranded RNA (ssRNA) imaging at the single-base level. **Aa**, Outline of the tip-enhanced Raman scattering (TERS) approach. **Ab**, Top, integral peak intensity at 1,370 cm^{-1} comprising multiple nucleobases bands. Bottom, four spectra acquired along the red arrow (spot 1) in part **Ab** at a step size of 0.5 nm. **Ac**, Measured sequence of 20 nucleobases along the strand in part **Ab** (top). The most probable bases are labelled at the bottom and compared to the real sequence. Mismatches are marked by the dashed boxes. **B**, TERS virus discrimination. **Ba**, Morphology and chemical composition of the coxsackie virus B3. **Bd**, Morphology and chemical composition of the H1N1 virus. **Bb**,**Be**, TERS mapping of the virus surface by discrete spectra acquisition at randomly selected grid positions (inset). Marker bands correspond to proteins (green lines), RNA (red lines) and lipids (blue lines). **Bc**,**Bf**, Continuous TERS spectrum accumulation during scanning of the tip across a representative surface area of each virus leads to unique TERS peak pattern representing the entire chemical virus composition. a.u., arbitrary units; exp., experimental; RNP, ribonucleoprotein. Parts **Ab** and **Ac** adapted with permission from ref. 161, American Chemical Society. Part **b** adapted with permission from ref. 162, PNAS.

Raman marker bands[158]. These experiments demonstrate the lateral resolution capabilities and strength of combining structurally sensitive spectroscopy, such as TERS. Although it is unlikely to replace current PCR-based DNA sequencing methods, this approach can be applied to sequencing any chainlike molecules, including proteins or sugars.

Virus detection and differentiation. TERS shows promise as an alternative tool for virus detection and differentiation on minute sample volumes, bypassing extensive material amplification steps required in PCR testing[162,163]. Preliminary TERS studies on different virus types, including H1N1 virus and coxsackie virus B3 (CVB3), have demonstrated the need for substantial TERS datasets of the entire nanoscale chemical heterogeneity across the virus surface (Fig. 5Ba,Bd), to overcome spectral variability based on nanoscale composition of virus surfaces[162] (Fig. 5Bb,Be). To accomplish a meaningful averaging, the number of individual TERS spectra must match the covered area. Conservatively, considering 1-nm-diameter TERS resolution this means that for a 100-nm-diameter virus at least 10,000 TERS spectra are required, which are time-consuming to obtain. Alternatively, viruses can be differentiated by averaging the spectral information in a single spectrum across a selected region of interest. Here the tip is constantly moved, and the spectral information is continuously collected. This way the resolution is artificially reduced and, hence, representative of chemical composition of the entire area of the scanned virus (Fig. 5Bc,Bf). TERS scans of the H1N1 virus provided information on the lipid and protein content, whereas CVB3 TERS spectra were distinguishable by RNA and protein content. However, the variability of single TERS spectra is inherent to high lateral resolution and surface composition, emphasizing the importance of the averaging procedure for applications such as virus discrimination. Point-by-point mapping would require a dense mapping grid, resulting in long acquisition times. Depending on the application one has can choose between a fast averaging at the cost of spatial resolution or a highly resolved experiment that can locally distinguish, for example, lipids and proteins.

Nanoscale chemical reactivity

TERS offers a powerful and efficient method for observing and controlling nanoscale chemical reactivity at specific reaction sites. TERS uses the intrinsic plasmon properties of the tip to localize and amplify electromagnetic fields for sensing, but it can also accelerate chemical reaction rates and control reaction products through hot electron and heat effects induced by the plasmons. Consequently, TERS serves as a valuable tool for elucidating nanoscale chemical reaction mechanisms, identifying specific molecular structures at the nanoscale, and even inducing novel specific reaction pathways.

Initial investigations using AFM-TERS focused on the plasmon-induced reaction of pNTP on gold nanoplates. Silver-coated tips were brought into contact with the pNTP monolayer on atomically flat gold nanoplates, and illumination of the tip–sample system facilitated the conversion of pNTP to dimercaptoazobenzene (DMAB). Time-dependent TERS spectra clearly depicted the decrease in the pNTP marker bands and the concomitant increase in the characteristic azo group signals of DMAB at 1,440 cm^{-1} (ref. 37) (Fig. 6). Subsequent in situ high-vacuum TERS (HV-TERS) experiments confirmed this chemical reaction under environmentally controlled conditions[38]. TERS technology, with its high detection sensitivity and precise tip control, is well-suited for determining the chemical properties and structure of materials at very high resolution. It enables characterization of electronic properties and catalytic activity of different sites on the surface with a spatial resolution of up to 3 nm have been shown[40]. TERS is also effective in characterizing nanoscale chemical reactions in both liquid environments and on solid–liquid interfaces[39]. Recent research indicates that TERS in high-vacuum environments can further enhance its potential for ultra-sensitive spectral analysis of chemical reactions at a nanoscale. By adjusting the tunnelling current, HV-TERS can effectively control the gap, enabling additional monitoring of surface catalytic reactions. The high-vacuum environment prevents contamination and facilitates high spatial resolution.

2D materials

One-atom or few-atoms thick 2D materials represent a new class of low-dimensional materials with applications in advanced electronics, optoelectronics, energy storage devices and twistronics[164,165]. Their electronic and optical properties are highly adaptable owing to sensitivity to internal (defects, impurities, stacking order, twist angle) and external (strain, doping)[166] influences on their electronic and phononic properties.

The quantum coherence length (L_C), a crucial property governing 2D materials, typically ranges from 1 to 100 nm but has not yet been established in the spatial domain. Unlike incoherent micro-Raman scattering, the spatial coherence of phonons and electrons in 2D materials controls TERS enhancement because L_C is comparable to a spatial field confinement. Thus, TERS is ideal for investigating nanoscale electrical and thermal transport mechanisms, defects, strain and doping effects of 2D materials[142,167–172]. Spatial coherence Raman scattering theory for 2D materials accounts for the non-radiating near-field components and identifies the coherence properties of the inelastically scattered field[173–175]. The occurring field interferences can be either constructive or destructive, depending on the sequence of the involved internal scattering processes, vibrational mode symmetry and dimensionality. Consequently, the TERS signal of different Raman modes can exhibit different amplification. Accordingly, when applying already-established micro-Raman metrological approaches to TERS datasets for quantitative property assessments, adjustments (for example, enhancement-specific corrections) are necessary as was demonstrated in a study quantifying defects in graphene[176].

Probing the Raman spatial coherence length of 2D materials. The TERS signal depends on the tip–sample distance, facilitating experimental nanoscale determination of the L_C via numerical fitting, yielding values of ~50–60 nm in GaS (ref. 177) and ~20–40 nm in graphene[174]. TERS coherence theory was validated using the Fermi-energy dependence of L_C (ref. 178), revealing to suppression of phonon-induced electronic excitations near the Dirac Point, with a subsequent shortening of L_C toward the neutrality point with decreasing doping levels[178].

Interpretation of the spatial correlation length in terms of phonons or electrons. Light scattering involves electron–light and electron–phonon coupling, raising questions about whether L_C is dictated by electron or phonon coherence length. The strength of TERS lies in gathering information near the Brillouin zone's centre, providing insights into the correlation of scattered electromagnetic field. Experimentally accessible phonon coherence length indirectly determines phonon group velocity[178], indicating the presence of ultrasharp kinks in phonon dispersion at the Brillouin zone centre. To date, calculations of the Kohn anomaly cannot confirm this behaviour[179,180], whereas the L_C experimentally determined values may be dictated by the electronic energy uncertainty rather than the phonon coherence length. Further research is needed to clarify its nature.

Localization of lattice dynamics and electrons in graphene heterostructures. Superlattice-forming van der Waals heterostructures yield specific intrinsic phonon properties that differ from regularly constructed 2D materials and can, therefore, be probed by TERS. TERS of reconstructed low-angle twisted bilayer graphene (rTBG) unveils lattice dynamics localization, such as strain solitons (SP) and topological (AA) points, separating triangular AB and BA stacked domains[181]. Although such structures cannot be imaged by AFM,

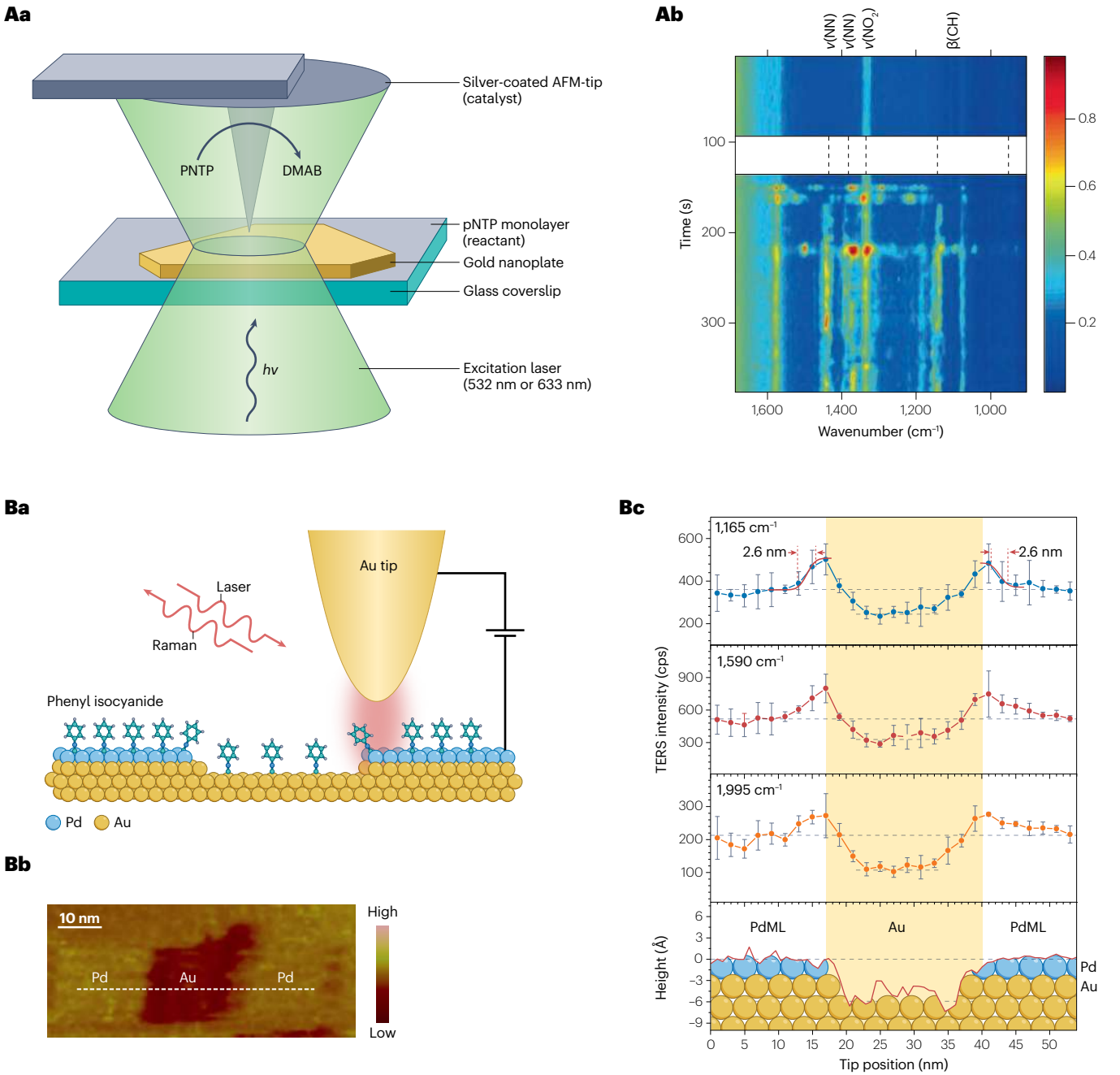

Fig. 6 | Application of TERS technology in nanoscale chemical reactivity. **A**, Catalytic processes of *p*-nitrothiophenol (pNTP) to dimercaptoazobenzene (DMAB) monitored at the nanoscale with atomic force microscopy combined with tip-enhanced Raman scattering (AFM-TERS). **Aa**, Photo-catalysed conversion of pNTP to DMAB by using the silver-coated AFM tip. **Ab**, Time-dependent TERS spectra of the catalytic processes before (top) and after (bottom) illumination at 633 nm. **B**, High-resolution scanning tunnelling microscopy (STM)-TERS study of the electronic and catalytic properties of a palladium(sub-monolayer)–gold(111) bimetallic system. **Ba**, STM-TERS using gold tips on palladium–gold(111) substrates coated with phenyl isocyanide molecules. **Bb**, STM image of the palladium–gold(111) phenyl isocyanide-coated surface. **Bc**, Height-correlated TERS intensities (1,165, 1,590 and 1,995 cm^{-1}) of phenyl isocyanide adsorbed on the surface palladium(sub-monolayer)–gold(111) bimetallic system. Error bars represent the standard deviation for each measurement. cps, counts per second. Parts **Aa** and **Ab** adapted from ref. 37, Springer Nature Limited. Part **B** adapted from ref. 40, Springer Nature Limited.

because they do not change the surface topography, the line shape of the 2D (G′) band is sensitive to electron localization and local electron–phonon coupling. While a typical 4 Lorentzian peak pattern is observed for AB stacked regions associated with the triangular domains (Fig. 7a,b), the SP–AA domains are characterized by a deviating line profile (Fig. 7c,d). Furthermore, the rTBG exhibits unique phonon properties such as a split G-phonon band (Fig. 7e,f), revealing insights into the influence of formed solitons and topological points on vibrational and electronic properties.

Local doping variations in lateral graphene homojunctions. Lateral graphene homojunctions formed of graphene@talc–graphene@SiO_2 consist of highly p-doped and lighter doped p′ areas, separated by a p–p′ junction (p′ < p) at the talc–SiO_2 interface (Fig. 7g). TERS investigations reveal abrupt changes in intensity, Raman shift and band width across interfacial regions[182]. Major contributing mechanism ascribes to doping effects rather than to strain, evidenced by 2D versus G frequency and intensity plot ratios. The 2D and G intensity ratio is inversely proportional to the charge doping, and so the talc supported graphene region shows a lower 2D/G intensity ratio compared to the SiO_2 supported region (Fig. 7h). Oscillation of the 2D/G intensity ratio across the interface suggests formation of a pp′pp′ junction, indicating local doping variations similar to diode pn junctions.

Reproducibility and data deposition

Achieving reproducibility in TERS experiments, particularly at the nanometre scale, presents unique challenges, owing to its highly localized measurement nature.

In TERS, as with any nanoscale experiment, there is an inherent inability to perform signal averaging at such a small scale. Unlike conventional macroscopic Raman spectroscopy, wherein signals from a relatively large sample volume allow for statistical averaging to minimize noise and enhance reproducibility, TERS experiments operate on an extremely localized level. The interaction volume between the tip and the sample is confined to the immediate vicinity of the nanoscale tip or even to a single atom-sized edge. Consequently, the Raman signal collected during TERS experiments lacks spatial averaging and is highly localized. Even small changes in the orientation of a molecule can lead to variations in the Raman signals, primarily owing to the extreme resolution of the technique rather than reproducibility issues. Although theoretical calculations can account for these effects, they complicate comparisons with existing databases typically used for spectrum assignment in Raman microscopy.

One approach to address these variations is to use averaging over larger areas if the extreme resolution is not essential. In many cases, a reduced lateral resolution of 10–20 nm is adequate, and in such instances, averaging over larger sub-areas, as demonstrated in the

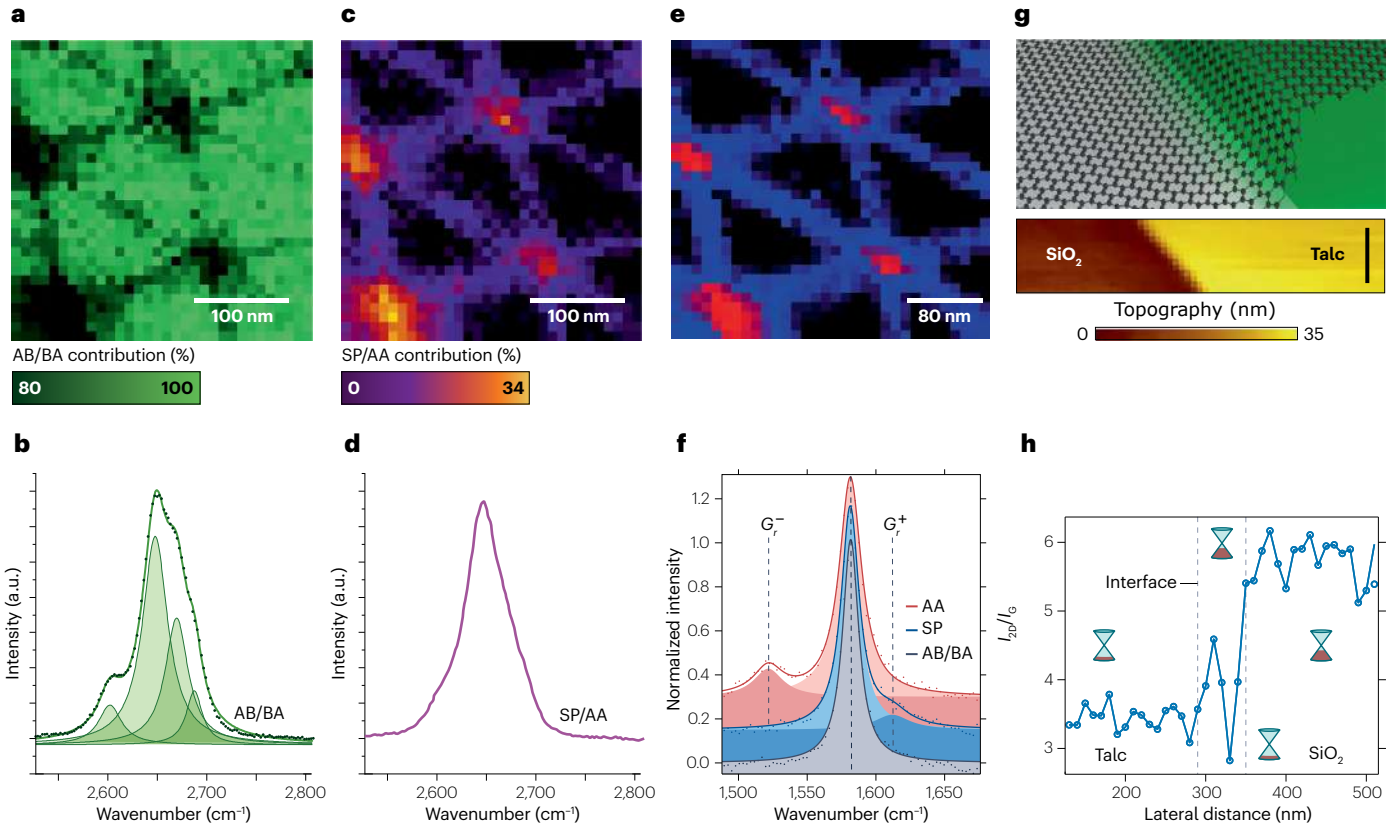

Fig. 7 | TERS imaging of reconstructed low-angle twisted bilayer graphene and lateral graphene homojunctions. a–**d**, Different 2D (G′) line profiles observed in the triangular AB/BA stacked regions as compared to the strain solitons and topological points separating the stacked regions. **e**,**f**, The G band exhibits new vibrational features that are also localized in space. **g**, Outline and atomic force microscopy (AFM) topography image of a pp′ junction in a lateral graphene@talc–graphene@SiO_2 homojunction. **h**, Evolution of the averaged 2D to G band intensity ratio across the interfacial region demonstrating the occurrence of oscillation associated with the formation of a pp′pp′ junction. a.u., arbitrary units; TERS, tip-enhanced Raman scattering. Parts **a**–**f** adapted from ref. 181, Springer Nature Limited. Parts **g** and **h** adapted from ref. 182, Springer Nature Limited.

Glossary

Adaptive optics
A technical approach to improve the quality of an optical system by reducing the wavefront distortions (increasing the phase matching) imposed by diffractive optical elements, light scattering in thick samples and the variation in the index of refraction along the light path by using deformable mirrors or liquid crystal spatial light modulators.

Boundary element methods
Methods to solve Maxwell's equation, which relies on the discretization of the surface elements of a configuration, wherein the boundary conditions are applied to each finite element of the elements of the interface.

Chemical effects
Stem from close-range and site-specific interactions between the surface-immobilized sample and the metallic nanoparticle and comprises non-resonant and resonant contributions and charge-transfer phenomena between the sample and the plasmonic nanoparticle.

Coherence length
The distance an electromagnetic wave can travel in a material and keeps its coherence, or maintain its phase.

Electromagnetic effect
Responsible for the locally confined and enhanced electric field and field gradients near the plasmonic particle.

Finite-difference time-domain methods
Grid-based differential numerical methods that allow to solve Maxwell's equations in an iterative scheme.

Finite element methods
Numerical approaches that can solve partial differential equations by dividing the system into a certain number of smaller subsystems (finite elements).

Force–volume AFM spectroscopy
An advanced imaging atomic force microscopy (AFM) mode enabling a quantification of certain nanomechanical properties (adhesion, stiffness, Young's modulus, dissipation and viscoelasticity) of a sample by recording entire extend-and-retract force–distance curves for each image pixel.

GPAW
A python implementation of the time-dependent density functional theory approach based on the projector augmented wave method.

Kohn anomaly
An anomaly in the phonon dispersion relation of graphene and metals, which arises from electron–phonon interaction, leading to a failure of the Born–Oppenheimer approximation.

Picocavity
Atomic-scale structure constituted by one or few metallic atoms protruding from the surface, which enables localization of light onto the atomic scale, often phrased as 'atomic protrusion'.

Polarizability tensor
Describes the induced dipole moment along one direction as a function of the local electric field in any given direction; according to the general selection rules in Raman spectroscopy, a vibration is Raman active only if the polarizability changes along the displacement vector of the specific vibrational normal mode.

Rayleigh line
Corresponds to the peak in a spectrum that arises from elastic scattering of the incident light in a sample, that is, at a frequency or energy corresponding to the incident light.

Spatial field confinement
The ability of a plasmonic nanostructure to convert free propagating radiation into localized energy, that is, the obtained spatial extension of the formed secondary electromagnetic filed at the tip apex.

Strain solitons
Nonlinear quasi-stationary localized strain waves in solids that occur at boundaries of symmetry-broken stacking domains (in the case of graphene, AB and BA stacking domains).

Synergistic TERS
A terminology to summarize comparative approaches pairing tip-enhanced Raman scattering (TERS) as a pivotal method with a secondary, ideally complementary analytical technique.

TERS virus example, is a viable approach. This differs from simply selecting larger step sizes for the TERS experiment, as that typically leads to inadequate sampling of the sample surface.

When comparing TERS experiments, the nature of scanning probe experiments must be considered. These experiments rely on the shape and properties of the tip, as well as the roughness of the specimen. Accurately capturing the topography of a sample depends on the sharpness of the tip. If the surface is too rough, the tip may not properly approach it, resulting in plasmonic enhancement and topography being registered at different locations on the tip, potentially misleading interpretations. Therefore, comparisons should only be made for smooth surfaces.

Currently, TERS-specific data repositories are unavailable, mirroring the absence of concise Raman or SERS repositories. Data are typically provided either as supplemental information or upon request from the authors of the respective publications. However, establishing TERS data repositories in the next decade is imperative to meet the demands of new artificial intelligence-based data analysis and interpretation methods. A web repository for microbiological Raman data, including TERS data, has been proposed[183]. These data analysis methods require precise, high-quality and reproducible datasets of sufficient volume. Given the complexity of parameter entanglement in TERS studies, establishing high entry requirements for these repositories is essential. These requirements depend on experimental parameters that must be carefully considered and defined according to field standards.

Limitations and optimizations

As one of the few methods capable of achieving nanoscale lateral resolution under ambient conditions, TERS stands out as a crucial tool for obtaining structural information about surfaces. However, this advantage comes with trade-offs. The extreme sensitivity and local resolution of TERS mean that it samples only a small number of molecules, resulting in highly surface-sensitive measurements. Consequently, TERS cannot directly access the bulk properties of a specimen. Like most scattering-type near-field optical techniques, TERS combines far-field and near-field contributions, necessitating careful measures to isolate the near-field signal. However, the far-field signal already offers an initial insight into bulk properties. Laser damage to the sample must also be considered, as is typical for any Raman setup.

The ultimate resolution limit of TERS remains unclear. Current experimental setups can localize the tip with a certain precision, depending on the feedback mechanism and general setup (cryogenic conditions, AFM or STM). Currently, a lateral resolution of less than 100 pm may be achieved. Theoretical considerations are particularly intriguing in this regard. The electromagnetic component of the Raman spectrum is linked to the excitation volume and determines the resolution limit. Conversely, the chemical effects contributing to the Raman spectrum depend solely on the precise positioning of the tip relative to the molecule. Therefore, the resolution is influenced by the technical precision and noise of the tip positioning, as well as the SNR of the collected Raman spectra. Although achieving resolution within the range of a bond length can be generally deemed sufficient from a chemical perspective, appropriate equipment might go below this scale.

Limitations in liquid

Using TERS to study biological samples requires technical solutions for investigating samples in their natural or native state. Liquid TERS bio-applications, although intriguing, remain uncommon. Previous liquid TERS investigations have focused on simple sample systems such as lipid monolayers and bilayers and protein fibrils, typically under physiologically irrelevant ambient conditions. To establish liquid TERS as a routine method, issues related to tips and feedback mechanisms must be addressed. STM-TERS in liquid environments requires special tip treatment to reduce Faradaic currents whereas AFM-TERS is preferred for biological matter. Liquid AFM-TERS introduces additional hydrodynamic and sample interaction forces, leading to altered molecular orientation and the occurrence of periodic hydration forces and Derjaguin–Landau–Verwey–Overbeek (DLVO) forces. Typically, the tip–sample distance increases for set points similar to ambient settings. Liquid TERS may encounter significant tip lifetime issues; metal-coated dielectric or semi-conducting tips exposed to aqueous solutions may experience partial detachment of the metal film or metal nanoparticles. Although intermediate adhesion layers can improve mechanical stability, the lifetime of TERS tips may still be significantly reduced owing to chemical damage by organic solvents, acids or buffer solutions. Tip contamination by residual analytes in the solution is also a potential issue. Introduction of additional thin protective layers can decrease the risk of chemical destruction and contamination, but careful material selection and thickness considerations are crucial for preserving enhancement capabilities.

Outlook

As the field develops, it continues to face challenges, such as improving reliability and accessibility; novel approaches, innovative technology and interdisciplinary collaboration are constantly driving the field forward. In this section, we explore the challenges in the TERS field, innovative approaches being developed, questions TERS can answer, priorities for the next decade and potential applications of TERS beyond its immediate domain.

Challenges in TERS research

Achieving stable, highly enhancing and reproducible TERS tips remains a challenge, especially for complex specimens such as those in biological sciences. Although the atomic-scale edge required is typically formed automatically, improving tip stability, particularly in challenging environments, is crucial. Leveraging existing scanning probe technologies for TERS experiments could be beneficial.

Intrinsic TERS signal variability owing to extreme localization dependency hinders quantitative assessment of sample composition. Developing standardized protocols, particularly for reduced resolution approaches, could enable breakthroughs based on correct local averaging.

Most TERS investigations are static, focusing on samples in equilibrium. Dynamic kinetic investigations could provide insights into reactivity on solid surfaces, such as catalytic reactions. Overcoming potential reactivity of the tip itself and acquisition restrictions of current setups is a primary challenge.

Innovative approaches in TERS research

Combining non-linear optical techniques such as coherent anti-Stokes Raman scattering and stimulated Raman scattering with tip enhancement offers dramatically improved sensitivity. Enhancements in measurement speed, such as picosecond-scale time resolutions and overcoming sample drift, are expected. Automatically matching the incoming light's field to specific tip requirements using spatial light modulators can substantially improve TERS signal intensity. This approach, along with non-linear optical methods, holds promise for improving measurement time. The application of artificial intelligence and machine learning principles in TERS spectra analysis could expedite spectrum assignment, ideally during experiments, leading to faster data interpretation.

Priorities for the next decade

Experimental and theoretical evaluation of the resolution limit of TERS or other TERS-based experiments under varying environmental conditions is paramount. Addressing experimental challenges and determining appropriate theoretical models are key aspects. Simplifying instrumentation systems is crucial for wider adoption of TERS across disciplines. Interdisciplinary collaborations are vital, and complex experimental setups may pose barriers to potential users.

Potential applications

TERS finds applications in a range of fields, from biological and pharmaceutical applications to solid-state physics. It enables the label-free study of surface structures beyond the optical diffraction limit, making it applicable in materials science, medical diagnostics, pharmaceutical analysis and environmental monitoring wherein target structures are smaller than 100 nm.

In conclusion, TERS holds immense potential as a tool for probing the nanoscale world, with ongoing research and innovative approaches driving the field forward. Its applications extend far beyond its immediate domain, promising transformative impacts across scientific and technological realms in the years to come.

Published online: 11 July 2024

References

1. Anderson, M. S. Locally enhanced Raman spectroscopy with an atomic force microscope. *Appl. Phys. Lett.* **76**, 3130–3132 (2000).
2. Hayazawa, N., Inouye, Y., Sekkat, Z. & Kawata, S. Metallized tip amplification of near-field Raman scattering. *Opt. Commun.* **183**, 333–336 (2000).
3. Stöckle, R. M., Suh, Y. D., Deckert, V. & Zenobi, R. Nanoscale chemical analysis by tip-enhanced Raman spectroscopy. *Chem. Phys. Lett.* **318**, 131–136 (2000).
4. Domke, K. F., Zhang, D. & Pettinger, B. Toward Raman fingerprints of single dye molecules at atomically smooth Au(111). *J. Am. Chem. Soc.* **128**, 14721–14727 (2006).
5. Neacsu, C. C., Dreyer, J., Behr, N. & Raschke, M. B. Scanning-probe Raman spectroscopy with single-molecule sensitivity. *Phys. Rev. B* **73**, 193406 (2006).
6. Zhang, W., Yeo, B. S., Schmid, T. & Zenobi, R. Single molecule tip-enhanced Raman spectroscopy with silver tips. *J. Phys. Chem. C* **111**, 1733–1738 (2007).

7. Richard-Lacroix, M., Zhang, Y., Dong, Z. & Deckert, V. Mastering high resolution tip-enhanced Raman spectroscopy: towards a shift of perception. *Chem. Soc. Rev.* **46**, 3922–3944 (2017).
8. Hartschuh, A., Sánchez, E. J., Xie, X. S. & Novotny, L. High-resolution near-field Raman microscopy of single-walled carbon nanotubes. *Phys. Rev. Lett.* **90**, 095503 (2003).
9. Chen, C., Hayazawa, N. & Kawata, S. A 1.7 nm resolution chemical analysis of carbon nanotubes by tip-enhanced Raman imaging in the ambient. *Nat. Commun.* **5**, 3312 (2014).
10. Anderson, N., Hartschuh, A. & Novotny, L. Chirality changes in carbon nanotubes studied with near-field Raman spectroscopy. *Nano Lett.* **7**, 577–582 (2007).
11. Anderson, N., Hartschuh, A., Cronin, S. & Novotny, L. Nanoscale vibrational analysis of single-walled carbon nanotubes. *J. Am. Chem. Soc.* **127**, 2533–2537 (2005).
12. Liao, M. et al. Tip-enhanced Raman spectroscopic imaging of individual carbon nanotubes with subnanometer resolution. *Nano Lett.* **16**, 4040–4046 (2016).
13. Yano, T.-A. et al. Tip-enhanced nano-Raman analytical imaging of locally induced strain distribution in carbon nanotubes. *Nat. Commun.* **4**, 2592 (2013).
14. Schultz, J. F. & Jiang, N. Characterizations of two-dimensional materials with cryogenic ultrahigh vacuum near-field optical microscopy in the visible range. *J. Vac. Sci. Technol. A* **40**, 40801 (2022).
This review article discusses the technical challenges and advantages of cryogenic UHV TERS and STM-induced luminescence.
15. Ren, B., Picardi, G., Pettinger, B., Schuster, R. & Ertl, G. Tip-enhanced Raman spectroscopy of benzenethiol adsorbed on Au and Pt single-crystal surfaces. *Angew. Chem. Int. Ed.* **44**, 139–142 (2005).
16. Wang, X. et al. Tip-enhanced Raman spectroscopy for investigating adsorbed species on a single-crystal surface using electrochemically prepared Au tips. *Appl. Phys. Lett.* **91**, 101105 (2007).
17. Chiang, N. et al. Conformational contrast of surface-mediated molecular switches yields Ångstrom-scale spatial resolution in ultrahigh vacuum tip-enhanced Raman spectroscopy. *Nano Lett.* **16**, 7774–7778 (2016).
18. Braun, K. et al. Probing bias-induced electron density shifts in metal–molecule interfaces via tip-enhanced Raman scattering. *J. Am. Chem. Soc.* **143**, 1816–1821 (2021).
19. Zhang, D., Domke, K. F. & Pettinger, B. Tip-enhanced Raman spectroscopic studies of the hydrogen bonding between adenine and thymine adsorbed on Au (111). *ChemPhysChem* **11**, 1662–1665 (2010).
20. Wang, X. et al. Revealing intermolecular interaction and surface restructuring of an aromatic thiol assembling on Au(111) by tip-enhanced Raman spectroscopy. *Anal. Chem.* **88**, 915–921 (2016).
21. Pandey, Y., Kumar, N., Goubert, G. & Zenobi, R. Nanoscale chemical imaging of supported lipid monolayers using tip-enhanced Raman spectroscopy. *Angew. Chem. Int. Ed.* **60**, 19041–19046 (2021).
22. Jiang, N. et al. Nanoscale chemical imaging of a dynamic molecular phase boundary with ultrahigh vacuum tip-enhanced Raman spectroscopy. *Nano Lett.* **16**, 3898–3904 (2016).
23. Kurouski, D., Deckert-Gaudig, T., Deckert, V. & Lednev, I. K. Structural characterization of insulin fibril surfaces using tip enhanced Raman spectroscopy (TERS). *Biophys. J.* **104**, 49A (2014).
24. Deckert-Gaudig, T. & Deckert, V. High resolution spectroscopy reveals fibrillation inhibition pathways of insulin. *Sci. Rep.* **6**, 39622 (2016).
25. Krasnoslobodtsev, A., Deckert-Gaudig, T., Zhang, Y., Deckert, V. & Lyubchenko, Y. L. Polymorphism of amyloid fibrils formed by a peptide from the yeast prion protein Sup35: AFM and tip-enhanced Raman scattering studies. *Ultramicroscopy* **165**, 26–33 (2016).
26. Paulite, M. et al. Full spectroscopic tip-enhanced Raman imaging of single nanotapes formed from β-amyloid(1-40) peptide fragments. *ACS Nano* **7**, 911–920 (2013).
27. Lipiec, E., Perez-Guaita, D., Kaderli, J., Wood, B. R. & Zenobi, R. Direct nanospectroscopic verification of the amyloid aggregation pathway. *Angew. Chem. Int. Ed.* **57**, 8519–8524 (2018).
28. Talaga, D. et al. Total internal reflection tip-enhanced Raman spectroscopy of tau fibrils. *J. Phys. Chem. B* **126**, 5024–5032 (2022).
29. Bonhommeau, S., Talaga, D., Hunel, J., Cullin, C. & Lecomte, S. Tip-enhanced Raman spectroscopy to distinguish toxic oligomers from Aβ1–42 fibrils at the nanometer scale. *Angew. Chem. Int. Ed.* **56**, 1771–1774 (2017).
30. D'Andrea, C. et al. Nanoscale discrimination between toxic and nontoxic protein misfolded oligomers with tip-enhanced Raman spectroscopy. *Small* **14**, 1800890 (2018).
31. vandenAkker, C. et al. Nanoscale heterogeneity of the molecular structure of individual hIAPP amyloid fibrils revealed with tip-enhanced Raman spectroscopy. *Small* **11**, 4131–4139 (2015).
32. Yeo, B.-S., Amstad, E., Schmid, T., Stadler, J. & Zenobi, R. Nanoscale probing of a polymer-blend thin film with tip-enhanced Raman spectroscopy. *Small* **5**, 952–960 (2009).
33. Xue, L. et al. High-resolution chemical identification of polymer blend thin films using tip-enhanced Raman mapping. *Macromolecules* **44**, 2852–2858 (2011).
34. Agapov, R. L., Scherger, J. D., Sokolov, A. P. & Foster, M. D. Identification of individual isotopes in a polymer blend using tip enhanced Raman spectroscopy. *J. Raman Spectrosc.* **46**, 447–450 (2015).
35. Höppener, C., Elter, J. K., Schacher, F. H. & Deckert, V. Inside block copolymer micelles — tracing interfacial influences on crosslinking efficiency in nanoscale confined spaces. *Small* **19**, 2206451 (2023).
36. Höppener, C., Schacher, F. H. & Deckert, V. Multimodal characterization of resin embedded and sliced polymer nanoparticles by means of tip-enhanced Raman spectroscopy and force-distance curve based atomic force microscopy. *Small* **112**, 1907418 (2020).
37. van Schrojenstein Lantman, E. M., Deckert-Gaudig, T., Mank, A. J. G., Deckert, V. & Weckhuysen, B. M. Catalytic processes monitored at the nanoscale with tip-enhanced Raman spectroscopy. *Nat. Nanotechnol.* **7**, 583–586 (2012).
38. Sun, M., Zhang, Z., Zheng, H. & Xu, H. In-situ plasmon-driven chemical reactions revealed by high vacuum tip-enhanced Raman spectroscopy. *Sci. Rep.* **2**, 647 (2012).
39. Pfisterer, J. H. K., Baghernejad, M., Giuzio, G. & Domke, K. F. Reactivity mapping of nanoscale defect chemistry under electrochemical reaction conditions. *Nat. Commun.* **10**, 5702 (2019).
40. Zhong, J.-H. et al. Probing the electronic and catalytic properties of a bimetallic surface with 3 nm resolution. *Nat. Nanotechnol.* **12**, 132–136 (2017).
41. Shao, F. et al. In-situ nanospectroscopic imaging of plasmon-induced two-dimensional [4+4]-cycloaddition polymerization on Au(111). *Nat. Commun.* **12**, 4557 (2021).
42. Mahapatra, S. et al. Localized surface plasmon controlled chemistry at and beyond the nanoscale. *Chem. Phys. Rev.* **4**, 021301 (2023).
43. Trautmann, S. et al. A classical description of subnanometer resolution by atomic features in metallic structures. *Nanoscale* **9**, 391–401 (2017).
44. Jakob, L. A. et al. Giant optomechanical spring effect in plasmonic nano- and picocavities probed by surface-enhanced Raman scattering. *Nat. Commun.* **14**, 3291 (2023).
45. García de Abajo, F. J. & Howie, A. Retarded field calculation of electron energy loss in inhomogeneous dielectrics. *Phys. Rev. B* **65**, 115418 (2002).
46. Hohenester, U. & Trügler, A. MNPBEM — a Matlab toolbox for the simulation of plasmonic nanoparticles. *Comput. Phys. Commun.* **183**, 370–381 (2012).
47. Cvitkovic, A., Ocelic, N., Aizpurua, J., Guckenberger, R. & Hillenbrand, R. Infrared imaging of single nanoparticles via strong field enhancement in a scanning nanogap. *Phys. Rev. Lett.* **97**, 060801 (2006).
48. Barbry, M. et al. Atomistic near-field nanoplasmonics: reaching atomic-scale resolution in nanooptics. *Nano Lett.* **15**, 3410–3419 (2015).
49. Schmidt, M. K., Esteban, R., González-Tudela, A., Giedke, G. & Aizpurua, J. Quantum mechanical description of Raman scattering from molecules in plasmonic cavities. *ACS Nano* **10**, 6291–6298 (2016).
50. Baumberg, J. J. Picocavities: a primer. *Nano Lett.* **22**, 5859–5865 (2022).
51. Benz, F. et al. Single-molecule optomechanics in "picocavities". *Science* **354**, 726–729 (2016).
52. Zhang, R. et al. Chemical mapping of a single molecule by plasmon-enhanced Raman scattering. *Nature* **498**, 82–86 (2013).
53. Lee, J., Crampton, K. T., Tallarida, N. & Apkarian, V. A. Visualizing vibrational normal modes of a single molecule with atomically confined light. *Nature* **568**, 78–82 (2019).
54. Jiang, S. et al. Subnanometer-resolved chemical imaging via multivariate analysis of tip-enhanced Raman maps. *Light Sci. Appl.* **6**, e17098 (2017).
55. Kong, F.-F. et al. Probing intramolecular vibronic coupling through vibronic-state imaging. *Nat. Commun.* **12**, 1280 (2021).
56. Hao, E. & Schatz, G. C. Electromagnetic fields around silver nanoparticles and dimers. *J. Chem. Phys.* **120**, 357–366 (2003).
57. Zou, S., Janel, N. & Schatz, G. C. Silver nanoparticle array structures that produce remarkably narrow plasmon lineshapes. *J. Chem. Phys.* **120**, 10871–10875 (2004).
58. Gieseking, R. L., Ratner, M. A. & Schatz, G. C. Semiempirical modeling of Ag nanoclusters: new parameters for optical property studies enable determination of double excitation contributions to plasmonic excitation. *J. Phys. Chem. A* **120**, 4542–4549 (2016).
59. Ding, W., Hsu, L.-Y., Heaps, C. W. & Schatz, G. C. Plasmon-coupled resonance energy transfer II: exploring the peaks and dips in the electromagnetic coupling factor. *J. Phys. Chem. C* **122**, 22650–22659 (2018).
60. Payton, J. L., Morton, S. M., Moore, J. E. & Jensen, L. A discrete interaction model/quantum mechanical method for simulating surface-enhanced Raman spectroscopy. *J. Chem. Phys.* **136**, 214103 (2012).
61. Payton, J. L., Morton, S. M., Moore, J. E. & Jensen, L. A hybrid atomistic electrodynamics — quantum mechanical approach for simulating surface-enhanced Raman scattering. *Acc. Chem. Res.* **47**, 88–99 (2014).
62. Hu, Z., Chulhai, D. V. & Jensen, L. Simulating surface-enhanced hyper-Raman scattering using atomistic electrodynamics-quantum mechanical models. *J. Chem. Theory Comput.* **12**, 5968–5978 (2016).
63. Liu, P., Chulhai, D. V. & Jensen, L. Single-molecule imaging using atomistic near-field tip-enhanced Raman spectroscopy. *ACS Nano* **11**, 5094–5102 (2017).
64. Chen, X., Liu, P., Hu, Z. & Jensen, L. High-resolution tip-enhanced Raman scattering probes sub-molecular density changes. *Nat. Commun.* **10**, 2567 (2019).
This research article introduces a theory adopting the concept of distributed polarizability density (namely, locally integrated Raman polarizability density (LIRPD)) to show that single-molecule TERS images can be explained by local sub-molecular density changes induced by extremely confined near-field interaction, and that these determine the obtainable TERS resolution and affect the Raman selection rules.
65. Schmidt, S. et al. Image formation properties and inverse imaging problem in aperture based scanning near field optical microscopy. *Opt. Express* **24**, 4128–4142 (2016).
66. Langer, J. et al. Present and future of surface-enhanced Raman scattering. *ACS Nano* **14**, 28–117 (2020).
67. Latorre, F. et al. Spatial resolution of tip-enhanced Raman spectroscopy — DFT assessment of the chemical effect. *Nanoscale* **8**, 10229–10239 (2016).
68. Rodriguez, R. D. et al. Chemical enhancement vs molecule–substrate geometry in plasmon-enhanced spectroscopy. *ACS Photonics* **8**, 2243–2255 (2021).
69. Fiederling, K., Kupfer, S. & Gräfe, S. Are charged tips driving TERS-resolution? A full quantum chemical approach. *J. Chem. Phys.* **154**, 034106 (2021).

70. Fiederling, K. et al. The chemical effect goes resonant — a full quantum mechanical approach on TERS. *Nanoscale* **12**, 6346–6359 (2020).
This research article presents a theoretical study of a tin(II) phthalocyanine molecule in the presence of a single silver atom utilizing a full quantum mechanical description to reveal unique non-resonant and resonant chemical tip–molecule interactions, and the research also demonstrates that these lead to alter TERS spectra and contribute to subnanometre TERS resolution.
71. Li, J., Li, X., Zhai, H.-J. & Wang, L.-S. Au_{20}: a tetrahedral cluster. *Science* **299**, 864–867 (2003).
72. Zhao, Jensen, L. & Schatz, G. C. Pyridine–Ag20 cluster: a model system for studying surface-enhanced Raman scattering. *J. Am. Chem. Soc.* **128**, 2911–2919 (2006).
73. Duan, S. et al. Theoretical modeling of plasmon-enhanced Raman images of a single molecule with subnanometer resolution. *J. Am. Chem. Soc.* **137**, 9515–9518 (2015).
74. Duan, S., Tian, G. & Luo, Y. Theory for modeling of high resolution resonant and nonresonant Raman images. *J. Chem. Theory Comput.* **12**, 4986–4995 (2016).
75. Duan, S., Xie, Z., Tian, G. & Luo, Y. Effects of plasmon modes on resonant Raman images of a single molecule. *J. Phys. Chem. Lett.* **11**, 407–411 (2020).
76. Mortensen, J. J., Hansen, L. B. & Jacobsen, K. W. Real-space grid implementation of the projector augmented wave method. *Phys. Rev. B* **71**, 035109 (2005).
77. Enkovaara, J. et al. Electronic structure calculations with GPAW: a real-space implementation of the projector augmented-wave method. *J. Phys. Condens. Matter* **22**, 253202 (2010).
78. Lin, Q. et al. Optical suppression of energy barriers in single molecule-metal binding. *Sci. Adv.* **8**, eabp9285 (2022).
79. Griffiths, J. et al. Resolving sub-Angstrom ambient motion through reconstruction from vibrational spectra. *Nat. Commun.* **12**, 6759 (2021).
80. Fiederling, K. et al. A full quantum mechanical approach assessing the chemical and electromagnetic effect in TERS. *ACS Nano* **17**, 13137–13146 (2023).
81. Zhang, Y., Dong, Z.-C. & Aizpurua, J. Theoretical treatment of single-molecule scanning Raman picoscopy in strongly inhomogeneous near fields. *J. Raman Spectrosc.* **52**, 296–309 (2021).
This paper introduces a simplified calculation procedure to calculate inhomogeneous field-enhanced Raman spectra from a single molecule.
82. Giovannini, T. et al. Do we really need quantum mechanics to describe plasmonic properties of metal nanostructures? *ACS Photonics* **9**, 3025–3034 (2022).
83. Bursi, L., Calzolari, A., Corni, S. & Molinari, E. Quantifying the plasmonic character of optical excitations in nanostructures. *ACS Photonics* **3**, 520–525 (2016).
84. Ropers, C. et al. Grating-coupling of surface plasmons onto metallic tips: a nanoconfined light source. *Nano Lett.* **7**, 2784–2788 (2007).
85. Berweger, S., Atkin, J. M., Olmon, R. L. & Raschke, M. Adiabatic tip-plasmon focusing for nano-Raman spectroscopy. *J. Phys. Chem. Lett.* **1**, 3427–3432 (2010).
86. Umakoshi, T., Saito, Y. & Verma, P. Highly efficient plasmonic tip design for plasmon nanofocusing in near-field optical microscopy. *Nanoscale* **8**, 5634–5640 (2016).
87. Lee, D. Y. et al. Adaptive tip-enhanced nano-spectroscopy. *Nat. Commun.* **12**, 3465 (2021).
88. Novotny, L., Bian, R. X. & Xie, X. S. Theory of nanometric optical tweezers. *Phys. Rev. Lett.* **79**, 645–648 (1997).
89. Kazemi-Zanjani, N., Vedraine, S. & Lagugne-Labarthet, F. Localized enhancement of electric field in tip-enhanced Raman spectroscopy using radially and linearly polarized light. *Opt. Express* **21**, 25271–25276 (2013).
90. Mueller, N. S., Juergensen, S., Höflich, K., Reich, S. & Kusch, P. Excitation-tunable tip-enhanced Raman spectroscopy. *J. Phys. Chem. C* **122**, 28273–28279 (2018).
91. Glebov, A. L. et al. Volume Bragg gratings as ultra-narrow and multiband optical filters. in *Proc. SPIE. 8428, Micro-Optics 2012* 84280C (2012).
92. Rapaport, A. et al. Very low frequency Stokes and anti-Stokes Raman spectra accessible with a single multichannel spectrograph and volume Bragg grating optical filters. *AIP Conf. Proc.* **1267**, 808–809 (2010).
93. Yano, T.-A., Ichimura, T., Kuwahara, S., Verma, P. & Kawata, S. Subnanometric stabilization of plasmon-enhanced optical microscopy. *Nanotechnology* **23**, 205503 (2012).
94. Yano, T.-A., Tsuchimoto, Y., Mochizuki, M., Hayashi, T. & Hara, M. Laser scanning-assisted tip-enhanced optical microscopy for robust optical nanospectroscopy. *Appl. Spectrosc.* **70**, 1239–1243 (2016).
95. Kato, R., Moriyama, T., Umakoshi, T., Yano, T.-A. & Verma, P. Ultrastable tip-enhanced hyperspectral optical nanoimaging for defect analysis of large-sized WS_2 layers. *Sci. Adv.* **8**, eabo4021 (2022).
96. Hayazawa, N., Furusawa, K. & Kawata, S. Nanometric locking of the tight focus for optical microscopy and tip-enhanced microscopy. *Nanotechnology* **23**, 465203 (2012).
97. Binnig, G., Quate, C. F. & Gerber, C. Atomic force microscope. *Phys. Rev. Lett.* **56**, 930–933 (1986).
98. Binnig, G., Rohrer, H., Gerber, C. & Weibel, E. Surface studies by scanning tunneling microscopy. *Phys. Rev. Lett.* **49**, 57–61 (1982).
99. Cappella, B. & Dietler, G. Force-distance curves by atomic force microscopy. *Surf. Sci. Rep.* **34**, 1–104 (1999).
100. Karrai, K. & Tiemann, I. Interfacial shear force microscopy. *Phys. Rev. B* **62**, 13174–13181 (2000).
101. Hansma, P. K. et al. Tapping mode atomic force microscopy in liquids. *Appl. Phys. Lett.* **64**, 1738–1740 (1994).
102. Dufrêne, Y. F. et al. Imaging modes of atomic force microscopy for application in molecular and cell biology. *Nat. Nanotechnol.* **12**, 295–307 (2017).
103. Xu, D., Liang, B., Xu, Y. & Liu, M. Recent advances in tip-enhanced Raman spectroscopy probe designs. *Nano Res.* **16**, 5555–5571 (2023).
104. Pettinger, B., Picardi, G., Schuster, R. & Ertl, G. Surface enhanced Raman spectroscopy: towards single molecule spectroscopy. *Electrochemistry* **68**, 942–949 (2000).
105. Yang, B., Kazuma, E., Yokota, Y. & Kim, Y. Fabrication of sharp gold tips by three-electrode electrochemical etching with high controllability and reproducibility. *J. Phys. Chem. C* **122**, 16950–16955 (2018).
106. Taguchi, A., Yu, J., Verma, P. & Kawata, S. Optical antennas with multiple plasmonic nanoparticles for tip-enhanced Raman microscopy. *Nanoscale* **7**, 17424–17433 (2015).
In this article, the authors theoretically and experimentally investigate the influence of multiple metal grains on the electromagnetic field enhancement.
107. Vasconcelos, T. L. et al. Tuning localized surface plasmon resonance in scanning near-field optical microscopy probes. *ACS Nano* **9**, 6297–6304 (2015).
108. Vasconcelos, T. L. et al. Plasmon-tunable tip pyramids: monopole nanoantennas for near-field scanning optical microscopy. *Adv. Optical Mater.* **6**, 1800528 (2018).
109. Carnegie, C. et al. Room-temperature optical picocavities below 1 nm^3 accessing single-atom geometries. *J. Phys. Chem. Lett.* **9**, 7146–7151 (2018).
This research article demonstrates the chemistry and dynamics of a single gold adatom, distinguishing atom dynamics in real time, to provide insights into the stability of picocavities under ambient conditions.
110. Huang, Y.-P. et al. Shell-isolated tip-enhanced Raman and fluorescence spectroscopy. *Angew. Chem. Int. Ed.* **57**, 7523–7527 (2018).
111. Martín Sabanés, N., Driessen, L. M. A. & Domke, K. F. Versatile side-illumination geometry for tip-enhanced Raman spectroscopy at solid/liquid interfaces. *Anal. Chem.* **88**, 7108–7114 (2016).
112. Yokota, Y. et al. Systematic assessment of benzenethiol self-assembled monolayers on Au(111) as a standard sample for electrochemical tip-enhanced Raman spectroscopy. *J. Phys. Chem. C* **123**, 2953–2963 (2019).
113. Chen, X., Goubert, G., Jiang, S. & Van Duyne, R. P. Electrochemical STM tip-enhanced Raman spectroscopy study of electron transfer reactions of covalently tethered chromophores on Au(111). *J. Phys. Chem. C* **122**, 11586–11590 (2018).
114. Kumar, N., Wondergem, C. S., Wain, A. J. & Weckhuysen, B. M. In situ nanoscale investigation of catalytic reactions in the liquid phase using zirconia-protected tip-enhanced Raman spectroscopy probes. *J. Phys. Chem. Lett.* **10**, 1669–1675 (2019).
115. Zeng, Z.-C. et al. Electrochemical tip-enhanced Raman spectroscopy. *J. Am. Chem. Soc.* **137**, 11928–11931 (2015).
116. Nečas, D. & Klapetek, P. Gwyddion: an open-source software for SPM data analysis. *Open Phys.* **10**, 181–188 (2012).
117. Kurouski, D., Mattei, M. & Van Duyne, R. Probing redox reactions at the nanoscale with electrochemical tip-enhanced Raman spectroscopy. *Nano Lett.* **15**, 7956–7962 (2015).
118. Zhang, Z., Deckert-Gaudig, T., Singh, P. & Deckert, V. Single molecule level plasmonic catalysis — a dilution study of p-nitrothiophenol on gold dimers. *Chem. Commun.* **51**, 3069–3072 (2015).
119. Zhang, Z., Richard-Lacroix, M. & Deckert, V. Plasmon induced polymerization using a TERS approach: a platform for nanostructured 2D/1D material production. *Faraday Discuss.* **205**, 213–226 (2017).
120. Szczerbiński, J., Metternich, J. B., Goubert, G. & Zenobi, R. How peptides dissociate in plasmonic hot spots. *Small* **16**, 1905197 (2020).
121. Veres, M., Füle, M., Tóth, S., Koós, M. & Pócsik, I. Surface enhanced Raman scattering (SERS) investigation of amorphous carbon. *Diam. Relat. Mater.* **13**, 1412–1415 (2004).
122. Yao, X. et al. Targeted suppression of peptide degradation in Ag-based surface-enhanced Raman spectra by depletion of hot carriers. *Small* **18**, 2205080 (2022).
123. Meng, L., Yang, Z., Chen, J. & Sun, M. Effect of electric field gradient on sub-nanometer spatial resolution of tip-enhanced Raman spectroscopy. *Sci. Rep.* **5**, 9240 (2015).
124. Sun, M., Zhang, Z., Chen, L., Sheng, S. & Xu, H. Plasmonic gradient effects on high vacuum tip-enhanced Raman spectroscopy. *Adv. Optical Mater.* **2**, 74–80 (2014).
125. Cao, Y. et al. Plasmonic gradient and plexcitonic effects in single-molecule tip-enhanced (resonance) Raman spectroscopy. *J. Phys. Chem. C* **127**, 476–489 (2023).
126. Poliani, E. et al. Breakdown of far-field Raman selection rules by light–plasmon coupling demonstrated by tip-enhanced Raman scattering. *J. Phys. Chem. Lett.* **8**, 5462–5471 (2017).
127. Deckert-Gaudig, T., Rauls, E. & Deckert, V. Aromatic amino acid monolayers sandwiched between gold and silver: a combined tip-enhanced Raman and theoretical approach. *J. Phys. Chem. C* **114**, 7412–7420 (2010).
128. Kurouski, D., Postiglione, T., Deckert-Gaudig, T., Deckert, V. & Lednev, I. K. Amide I vibrational mode suppression in surface (SERS) and tip (TERS) enhanced Raman spectra of protein specimens. *Analyst* **138**, 1665–1673 (2013).
129. Liu, S., Hammud, A., Wolf, M. & Kumagai, T. Atomic point contact Raman spectroscopy of a Si(111)-7 × 7 surface. *Nano Lett.* **21**, 4057–4061 (2021).
130. Yang, B. et al. Chemical enhancement and quenching in single-molecule tip-enhanced Raman spectroscopy. *Angew. Chem. Int. Ed.* **62**, e202218799 (2023).
131. Guo, S., Popp, J. & Bocklitz, T. Chemometric analysis in Raman spectroscopy from experimental design to machine learning-based modeling. *Nat. Protoc.* **16**, 5426–5459 (2021).
132. Gautam, R., Vanga, S., Ariese, F. & Umapathy, S. Review of multidimensional data processing approaches for Raman and infrared spectroscopy. *EPJ Tech. Instrum.* **2**, 8 (2015).
133. Su, W., Kumar, N., Krayev, A. & Chaigneau, M. In situ topographical chemical and electrical imaging of carboxyl graphene oxide at the nanoscale. *Nat. Commun.* **9**, 2891 (2018).
This work introduces multi-parameter microscopy to measure local electronic properties in situ by KPFM.

134. Deckert-Gaudig, T., Pichot, V., Spitzer, D. & Deckert, V. High-resolution Raman spectroscopy for the nanostructural characterization of explosive nanodiamond precursors. *ChemPhysChem* **18**, 175–178 (2017).
135. Dou, T., Li, Z., Zhang, J., Evilevitch, A. & Kurouski, D. Nanoscale structural characterization of individual viral particles using atomic force microscopy infrared spectroscopy (AFM-IR) and tip-enhanced Raman spectroscopy (TERS). *Anal. Chem.* **92**, 11297–11304 (2020).
136. Hermelink, A. et al. Towards a correlative approach for characterising single virus particles by transmission electron microscopy and nanoscale Raman spectroscopy. *Analyst* **142**, 1342–1349 (2017).
137. Huang, S.-C. et al. Electrochemical tip-enhanced Raman spectroscopy: an in situ nanospectroscopy for electrochemistry. *Annu. Rev. Phys. Chem.* **72**, 213–234 (2021).
This research article provides a review on electrochemical TERS.
138. Yokota, Y., Hong, M., Hayazawa, N. & Kim, Y. Electrochemical tip-enhanced Raman spectroscopy for microscopic studies of electrochemical interfaces. *Surf. Sci. Rep.* **77**, 100576 (2022).
139. Pfisterer, J. H. K. & Domke, K. F. Unfolding the versatile potential of EC-TERS for electrocatalysis. *Curr. Opin. Electrochem.* **8**, 96–102 (2018).
140. Martín Sabanés, N., Ohto, T., Andrienko, D., Nagata, Y. & Domke, K. F. Electrochemical TERS elucidates potential-induced molecular reorientation of adenine/Au(111). *Angew. Chem. Int. Ed.* **56**, 9796–9801 (2017).
141. Fiocco, A. et al. Electrochemical tip-enhanced Raman spectroscopy for the elucidation of complex electrochemical reactions. *Anal. Chem.* **96**, 2791–2798 (2024).
142. Smithe, K. K. H. et al. Nanoscale heterogeneities in monolayer $MoSe_2$ revealed by correlated scanning probe microscopy and tip-enhanced Raman spectroscopy. *ACS Appl. Nano Mater.* **1**, 572–579 (2018).
143. Bonhommeau, S., Cooney, G. S. & Huang, Y. Nanoscale chemical characterization of biomolecules using tip-enhanced Raman spectroscopy. *Chem. Soc. Rev.* **51**, 2416–2430 (2022).
This review article focuses specifically on TERS applications related to biomatter, and it critically discusses challenges related to this field.
144. Talaga, D. et al. PIP2 phospholipid-induced aggregation of tau filaments probed by tip-enhanced Raman spectroscopy. *Angew. Chem. Int. Ed.* **57**, 15738–15742 (2018).
145. Lipiec, E. et al. Nanoscale hyperspectral imaging of amyloid secondary structures in liquid. *Angew. Chem. Int. Ed.* **60**, 4545–4550 (2021).
This recent TERS study comprises the successful integration of liquid TERS for probing the secondary structure of amyloid fibrils in situ.
146. Wood, B. R. et al. Tip-enhanced Raman scattering (TERS) from hemozoin crystals within a sectioned erythrocyte. *Nano Lett.* **11**, 1868–1873 (2011).
147. Mrđenović, D., Ge, W., Kumar, N. & Zenobi, R. Nanoscale chemical imaging of human cell membranes using tip-enhanced Raman spectroscopy. *Angew. Chem. Int. Ed.* **61**, e202210288 (2022).
148. Tabatabaei, M., Caetano, F. A., Pashee, F., Ferguson, S. S. G. & Lagugné-Labarthet, F. Tip-enhanced Raman spectroscopy of amyloid β at neuronal spines. *Analyst* **142**, 4415–4421 (2017).
149. Stepanenko, T. et al. Surface-enhanced Raman scattering (SERS) and tip-enhanced Raman scattering (TERS) in label-free characterization of erythrocyte membranes and extracellular vesicles at the nano-scale and molecular level. *Analyst* **149**, 778–788 (2024).
150. Alexander, K. D. & Schultz, Z. D. Tip-enhanced Raman detection of antibody conjugated nanoparticles on cellular membranes. *Anal. Chem.* **84**, 7408–7414 (2012).
151. Xiao, L., Wang, H. & Schultz, Z. D. Selective detection of RGD-integrin binding in cancer cells using tip enhanced Raman scattering microscopy. *Anal. Chem.* **88**, 6547–6553 (2016).
152. Domke, K., Zhang, D. & Pettinger, B. Tip-enhanced Raman spectra of picomole quantities of DNA nucleobases at Au (111). *J. Am. Chem. Soc.* **129**, 6708–6709 (2007).
153. Watanabe, H., Ishida, Y., Hayazawa, N., Inouye, Y. & Kawata, S. Tip-enhanced near-field Raman analysis of tip-pressurized adenine molecule. *Phys. Rev. B* **69**, 155418 (2004).
154. Bailo, E. & Deckert, V. Tip-enhanced Raman spectroscopy of single RNA strands: towards a novel direct-sequencing method. *Angew. Chem. Int. Ed.* **47**, 1658–1661 (2008).
155. Lin, X. et al. Direct base-to-base transitions in ssDNA revealed by tip-enhanced Raman scattering. Preprint at https://doi.org/10.48550/arXiv.1604.06598 (2016).
156. Hennemann, L. E., Meixner, A. J. & Zhang, D. Surface- and tip-enhanced Raman spectroscopy of DNA. *Spectroscopy* **24**, 119–124 (2010).
157. Treffer, R., Lin, X.-M., Bailo, E., Deckert-Gaudig, T. & Deckert, V. Distinction of nucleobases — a tip-enhanced Raman spectroscopy approach. *Beilstein J. Nanotechnol.* **2**, 628–637 (2011).
158. Najjar, S. et al. Tip-enhanced Raman spectroscopy of combed double-stranded DNA bundles. *J. Phys. Chem. C* **118**, 1174–1181 (2013).
159. Zhang, R. et al. Distinguishing individual DNA bases in a network by non-resonant tip-enhanced Raman scattering. *Angew. Chem. Int. Ed.* **56**, 5561–5564 (2017).
160. He, Z. et al. Tip-enhanced Raman imaging of single-stranded DNA with single base resolution. *J. Am. Chem. Soc.* **141**, 753–757 (2019).
This TERS study proves subnanometre resolution under ambient conditions by direct nucleic acid sequencing of a phage ssDNA at a step size of 0.5 nm.
161. He, Z. et al. Resolving the sequence of RNA strands by tip-enhanced Raman spectroscopy. *ACS Photonics* **8**, 424–430 (2021).
162. Deckert, V. et al. Laser spectroscopic technique for direct identification of a single virus I: FASTER CARS. *Proc. Natl Acad. Sci. USA* **117**, 27820–27824 (2020).
163. Olschewski, K. et al. A manual and an automatic TERS based virus discrimination. *Nanoscale* **7**, 4545–4552 (2015).
164. Geim, A. K. & Novoselov, K. S. The rise of graphene. *Nat. Mater.* **6**, 183–191 (2007).
165. Geim, A. K. Graphene: status and prospects. *Science* **324**, 1530–1534 (2009).
166. Malard, L. M. et al. Studying 2D materials with advanced Raman spectroscopy: CARS, SRS and TERS. *Phys. Chem. Chem. Phys.* **23**, 23428–23444 (2021).
167. Rahaman, M. et al. Highly localized strain in a MoS_2/Au heterostructure revealed by tip-enhanced Raman spectroscopy. *Nano Lett.* **17**, 6027–6033 (2017).
168. Vantasin, S. et al. Tip-enhanced Raman scattering of the local nanostructure of epitaxial graphene grown on 4H-SiC (000$\bar{1}$). *J. Phys. Chem. C* **118**, 25809–25815 (2014).
169. Su, W., Kumar, N., Mignuzzi, S., Crain, J. & Roy, D. Nanoscale mapping of excitonic processes in single-layer MoS_2 using tip-enhanced photoluminescence microscopy. *Nanoscale* **8**, 10564–10569 (2016).
170. Kato, R., Umakoshi, T., Sam, R. T. & Verma, P. Probing nanoscale defects and wrinkles in MoS_2 by tip-enhanced Raman spectroscopic imaging. *Appl. Phys. Lett.* **114**, 073105 (2019).
171. Huang, T.-X. et al. Probing the edge-related properties of atomically thin MoS_2 at nanoscale. *Nat. Commun.* **10**, 5544 (2019).
This research article demonstrates how TERS is used to probe the unique electronic property of defects in MoS_2.
172. Beams, R., Cançado, L. G., Jorio, A., Vamivakas, A. N. & Novotny, L. Tip-enhanced Raman mapping of local strain in graphene. *Nanotechnology* **26**, 175702 (2015).
173. Cançado, L. G., Beams, R., Jorio, A. & Novotny, L. Theory of spatial coherence in near-field Raman scattering. *Phys. Rev. X* **4**, 031054 (2014).
174. Publio, B. C. et al. Inclusion of the sample-tip interaction term in the theory of tip-enhanced Raman spectroscopy. *Phys. Rev. B* **105**, 235414 (2022).
175. Beams, R., Cançado, L. G., Oh, S.-H., Jorio, A. & Novotny, L. Spatial coherence in near-field Raman scattering. *Phys. Rev. Lett.* **113**, 186101 (2014).
176. Rabelo, C. et al. Linkage between micro- and nano-Raman spectroscopy of defects in graphene. *Phys. Rev. Appl.* **14**, 024056 (2020).
177. Alencar, R. S. et al. Probing spatial phonon correlation length in post-transition metal monochalcogenide gas using tip-enhanced Raman spectroscopy. *Nano Lett.* **19**, 7357–7364 (2019).
178. Nadas, R. B. et al. Spatially coherent tip-enhanced Raman spectroscopy measurements of electron–phonon interaction in a graphene device. *Nano Lett.* **23**, 8827–8832 (2023).
179. Piscanec, S., Lazzeri, M., Mauri, F., Ferrari, A. C. & Robertson, J. Kohn anomalies and electron-phonon interactions in graphite. *Phys. Rev. Lett.* **93**, 185503 (2004).
180. Das, A. et al. Monitoring dopants by Raman scattering in an electrochemically top-gated graphene transistor. *Nat. Nanotechnol.* **3**, 210–215 (2008).
181. Gadelha, A. C. et al. Localization of lattice dynamics in low-angle twisted bilayer graphene. *Nature* **590**, 405–409 (2021).
182. Gadelha, A. C., Vasconcelos, T. L., Cançado, L. G. & Jorio, A. Nano-optical imaging of in-plane homojunctions in graphene and MoS_2 van der Waals heterostructures on talc and SiO_2. *J. Phys. Chem. Lett.* **12**, 7625–7631 (2021).
183. Lee, K. S. et al. MicrobioRaman: an open-access web repository for microbiological Raman spectroscopy data. *Nat. Microbiol.* **9**, 1152–1156 (2024).
184. Baumberg, J. J., Aizpurua, J., Mikkelsen, M. H. & Smith, D. R. Extreme nanophotonics from ultrathin metallic gaps. *Nat. Mater.* **18**, 668–678 (2019).
185. Stanciu, C., Sackrow, M. & Meixner, A. J. High NA particle- and tip-enhanced nanoscale Raman spectroscopy with a parabolic-mirror microscope. *J. Microsc.* **229**, 247–253 (2008).
186. Stockman, M. I. Nanofocusing of optical energy in tapered plasmonic waveguides. *Phys. Rev. Lett.* **93**, 137404 (2004).
187. Gramotnev, D. K. & Bozhevolnyi, S. I. Nanofocusing of electromagnetic radiation. *Nat. Photonics* **8**, 13–22 (2014).
This review article provides an overview on the physical principles, developments and applications of nanofocusing in plasmonic nanostructures.
188. Lindquist, N. C., Nagpal, P., Lesuffleur, A., Norris, D. J. & Oh, S.-H. Three-dimensional plasmonic nanofocusing. *Nano Lett.* **10**, 1369–1373 (2010).
189. Taguchi, K., Umakoshi, T., Inoue, S. & Verma, P. Broadband plasmon nanofocusing: comprehensive study of broadband nanoscale light source. *J. Phys. Chem. C* **125**, 6378–6386 (2021).
190. Hampson, K. M. et al. Adaptive optics for high-resolution imaging. *Nat. Rev. Methods Primers* **1**, 68 (2021).
191. Umakoshi, T., Kawashima, K., Moriyama, T., Kato, R. & Verma, P. Tip-enhanced Raman spectroscopy with amplitude-controlled tapping-mode AFM. *Sci. Rep.* **12**, 12776 (2022).
192. Bartolomeo, G. L., Zhang, Y., Kumar, N. & Zenobi, R. Molecular perturbation effects in AFM-based tip-enhanced Raman spectroscopy: contact versus tapping mode. *Anal. Chem.* **93**, 15358–15364 (2021).

Acknowledgements

V.D. and C.H. acknowledge funding from the Deutsche Forschungsgemeinschaft (DFG, German Research Foundation) — CRC 1278 PolyTarget, project number 316213987 (project B04) and SFB 1375 (39881677, project C2). S.G. gratefully acknowledges funding from the European Research Council (ERC) under the European's Horizon 2020 research and innovation programme — QUEM-CHEM (grant number 772676), 'Time- and space-resolved ultrafast dynamics in molecular plasmonic hybrid systems' and by the DFG (German Research Foundation) — SFB 1375 (39881677, project A4). A.J. acknowledges support from FAPEMIG (APQ-01860-2229868, RED0008123) and CNPq (307619/2023-0, APQ-04852-23, 421469/2023-4), Brazil. J.A. acknowledges support from grant PID2022-139579NB-I00 of the Spanish Ministry of Science and Innovation and grant number IT 1526-22 from the Department of Education of the Basque Government. C.H. and Z.Z. acknowledge support from the

National Natural Science Foundation of China (numbers U22A6005 and 12304426) and the Natural Science Foundation of Shaanxi Province (numbers 2024JC-JCQN-07 and 22JSZ010).

Author contributions

Introduction (C.H., S.G., S.K., J.A. and V.D.); Experimentation (C.H., H.C., Z.Z. and V.D.); Results (C.H. and V.D.); Applications (C.H., A.J., H.C., Z.Z. and V.D.); Reproducibility and data deposition (C.H. and V.D.); Limitations and optimizations (C.H. and V.D.); Outlook (C.H., J.A., H.C., S.G., A.J., S.K., Z.Z. and V.D.); overview of the Primer (C.H., J.A., H.C., S.G., A.J., S.K., Z.Z. and V.D.).

Competing interests

The authors declare no competing interests.

Additional information

Peer review information *Nature Reviews Methods Primers* thanks the anonymous reviewer(s) for their contribution to the peer review of this work.